Geophysical Journal International

Geophys. J. Int. (2013) **195,** 1102–1119
Advance Access publication 2013 August 7

doi: 10.1093/gji/ggt273

Seismic energy envelopes in volcanic media: in need of boundary conditions

L. De Siena,[1] E. Del Pezzo,[2,*] C. Thomas,[1] A. Curtis[3] and L. Margerin[4]

[1] *University of Münster, Institut für Geophysik, Correnstrasse* 24, 48149 *Münster, Germany. E-mail: lucadesiena@uni-muenster.de*
[2] *Istituto Nazionale di Geofisica e Vulcanologia, sezione di Napoli "Osservatorio Vesuviano", Via Diocleziano* 328, 80124 *Naples, Italy*
[3] *School of GeoSciences, The University of Edinburgh, Grant Institute, The King's Buildings, Edinburgh EH*9 3*JW, UK.*
[4] *Institut de Recherche en Astrophysique et Planétologie, CNRS, Université de Toulouse, Observatoire Midi-Pyrénées,* 14 *Avenue Edouard Belin,* 31400 *Toulouse, France*

Accepted 2013 July 9. Received 2013 June 5; in original form 2012 May 4

Downloaded from http://gji.oxfordjournals.org/ at University of Edinburgh on December 28, 2013

SUMMARY

Seismogram envelopes recorded at Campi Flegrei caldera show diffusive characteristics as well as steep amplitude increases in the intermediate and late coda, which can be related to the presence of a non-uniformly scattering medium. In this paper, we first show the results of a simulation with a statistical model considering anisotropic scattering interactions, in order to match coda-envelope duration and shape. We consider as realistic parameters for a volcanic caldera the presence of large square root velocity fluctuations (10 per cent) and two typical correlation lengths for such an heterogeneous crust, $a = 0.1$ and 1 km. Then, we propose the inclusion of a diffusive boundary condition in the stochastic description of multiple scattering, in order to model intermediate and late coda intensities, and particularly the sharp intensity peaks at some stations in the caldera. Finally, we show that a reliable 2-D synthetic model of the envelopes produced by earthquakes vertically sampling a small region can be obtained including a single drastic change of the scattering properties of the volcano, that is, a caldera rim of radius 3 km, and sections varying between 2 and 3 km. These boundary conditions are diffusive, which signifies that the rim must have more scattering potential than the rest of the medium, with its diffusivity 2–3 orders of magnitude lower than the one of the background medium, so that the secondary sources on its interface(s) could enhance coda intensities. We achieve a good first-order model of high-frequency (18 Hz) envelope broadening adding to the Monte Carlo solution for the incident flux the secondary source effects produced by a closed annular boundary, designed on the caldera rim signature at 1.5 km depth. At lower frequencies (3 Hz) the annular boundary controls the intermediate and late coda envelope behaviour, in a way similar to an extended diffusive source. In our interpretation, the anomalous intensities observed at several stations and predicted by the final Monte Carlo solutions are mainly due to the diffusive transmission reflection from a scattering object of increased scattering power, and are controlled by its varying thickness.

Key words: Numerical solutions; Seismic anisotropy; Seismic attenuation; Seismic tomography; Wave scattering and diffraction; Calderas.

1 INTRODUCTION

Radiative transfer theory describes the transport of energy through a scattering medium; it is one of the most important tools to synthesize seismic coda intensities, the main evidence of scattering in the Earth (Wu 1985). Radiative transfer solutions provide theoretical energy coda envelopes that are comparable with experimental data; these envelopes, usually calculated as the mean square or the rms of coda signals, are crucial measurements of the degree of inhomogeneity of the Earth (Sato & Fehler 1998). For scalar waves, radiative transfer theory provides exact analytical solutions for isotropic scattering in two or four dimensions as well as approximate 3-D solutions (Paasschens 1997).

Single scattering and diffusion are asymptotic approximations of the transport equations often used to infer critical scattering parameters, such as the transport mean free path or the ratio between mean square fluctuations and correlation distance (Sato & Fehler 1998; Wegler & Lühr 2001; Przybilla *et al.* 2009). When dealing with a tenuous distribution of particles (where tenuous refers to

*Also at: Istituto Andaluz de Geofisica, Universidad de Granada, Granada, Spain.

© The Authors 2013. Published by Oxford University Press on behalf of The Royal Astronomical Society.

the particle density) single isotropic scattering solutions are used to model energy envelopes at regional scale (Sato 1977; Wu 1985). The single scattering approximation gives incorrect results in a medium with strong velocity fluctuations, and diffusion theory is a more suitable choice to describe scattered wave propagation in volcanic areas, at least in the presence of strong topography (Wegler & Lühr 2001). By using the diffusion approximation, Margerin *et al.* (1998) propose a boundary condition for the half-space including deterministic reflections. Wegler (2005) improves these conditions connecting a strongly scattering layer to a weakly scattering half-space. This last condition fails only if the thickness of the strong scattering layer is smaller than the transport mean free path and/or when a strong scattering contrast between the two layers exists. Nevertheless, one can still observe interference effects such as weak localization, which exists whether or not the scattering is weak or strong (Larose *et al.* 2004). Recently, Yamamoto & Sato (2010) presented clear observational evidences of mode conversions and multiple scattering at Asama volcano, which suggest that radiative transfer theory can be a preferable model to fit intensities even in a volcanic cone.

Except when analytic solutions exist, Monte Carlo numerical simulations of the radiative transfer equations are used to synthesize seismic envelopes (e.g. Gusev & Abubakirov 1987; Hoshiba 1991; Margerin *et al.* 1998, 2000; Yoshimoto 2000). Polarization information and broadening of the envelope are included in these techniques in order to obtain solutions modelled on real envelopes at regional scale (Margerin *et al.* 2000; Przybilla *et al.* 2006; Przybilla & Korn 2008). When used to describe energy propagation at teleseismic distances, Monte Carlo solutions provide important constraints on the Earth structure and behaviour, for example, through the analysis of PKP precursors (Margerin & Nolet 2003). On the other hand, when comparing the Monte Carlo simulated envelopes with real envelopes produced by a shallow volcano-tectonic earthquakes, random inhomogeneity with diffusive characteristics must be taken into account (Wegler 2005; Del Pezzo 2008). The coda decay in a volcanic region can be quantitatively well explained if the scattering coefficient changes with depth, even if leakage of scattered energy to the bottom of a bounded region cannot be discriminated from intrinsic loss (Parsieglia & Wegler 2008). In addition, the Earth properties can change in presence of lateral variations of the scattering properties, for volcanic fronts or mountain ranges (Yoshimoto *et al.* 2006; Sens-Schönfelder *et al.* 2009).

In their scattering tomography at Campi Flegrei Tramelli *et al.* (2006) show a dramatic lateral increase in the scattering power in a given part of the medium, induced, in their interpretation, by the presence of the old caldera rim. In their 2-D scattering tomography, De Siena *et al.* (2011) suggest that the scattering power of the Western caldera is higher than the one of the Eastern caldera, with the boundary between two media of different scattering powers located on the signature of the old caldera rim at 2 km depth (Zollo *et al.* 2003; Tramelli *et al.* 2006; Battaglia *et al.* 2008). With such a difference in scattering power, and many evidences of strong lateral changes in the velocity field, a standard scattering propagation model using lithospheric parameters may fail in modelling the volcanic envelopes at Campi Flegrei. Hence, we couple a standard Monte Carlo scheme and the diffusion approximation to model strong wave scattering inside the caldera rim. The diffusion process is essentially characterized by the time spent travelling inside the highly scattering medium—the rim—which acts as a trap, and redistributes the energy of the waves much like an extended resonant scatterer (Margerin 2013). The only quantity controlling this process is the natural characteristic timescale τ, that is, the Thouless time (Akkermans & Montambaux 2007, p. 156) dependent on the relative size of the system and on its diffusivities.

The scope of this paper is to obtain a first order Monte Carlo model of the seismic energy envelopes based on those at Campi Flegrei caldera. We want to understand if it is possible to reproduce the anomalous intensities observed in the intermediate coda by implementing a full 2-D elastic Monte Carlo simulation of the intensity produced by an extended source, after defining the single scattering coefficients *a priori*, using a von Kármán autocorrelation function and typical lithospheric parameters (Sato *et al.* 2004; Przybilla *et al.* 2006). The onset of the diffusion regime and the drastic intensity increase in the envelopes are investigated by comparing the synthetic results with the real coda envelopes. Finally, a large change in the distribution of the scatterers with respect to the average scattering medium is included to model the anomalous intensities and the whole broadened coda envelope behaviour. This change mainly requires the presence of a highly scattering area (e.g. the rim) which works as an additional wall, controlling the envelope shape and amplitude at intermediate times. Its implementation requires a spatial change in the medium physical parameters, that must necessarily be described in terms of a diffusive process.

2 DATA

We use the high frequency velocity recordings of 11 short-period three-component seismic stations installed by the University of Wisconsin inside the Campi Flegrei caldera (located in Southern Italy, Figs 1–3) during the 1982–1984 seismic crisis (e.g. Pujol & Aster 1990). In this period, a large number of low magnitude volcano-tectonic earthquakes were located in a cube of approximately 1-km-side length in the centre of the caldera (Aster *et al.* 1989; Saccorotti *et al.* 2007). The seismicity was later relocated using non-linear location algorithms (Lomax *et al.* 2001) while the corresponding waveforms were used by different authors to obtain velocity, attenuation, and scattering images of the caldera (De Lorenzo *et al.* 2001; Zollo *et al.* 2002; Tramelli *et al.* 2006; Battaglia *et al.* 2008; De Siena *et al.* 2010).

From these data we selected 212 waveforms recorded at various stations and produced by 59 earthquakes located in the 1 km^3 cube (the seismicity is shown in Figs 1 and 2). For each event-station pair we trace rays with the ray-bending approach of Block (1991) in the 3-D velocity structure of Battaglia *et al.* (2008). We then perform a 3-D *RTZ* rotation of the seismic waveforms in the along-path and transverse directions, employing both vertical and horizontal recordings, and compute the rms envelopes of the seismograms in the path and transverse directions (Sato & Fehler 1998; Levander & Nolet 2005). The transverse envelopes are the average of the *Z*- and *T*-components. Finally, we shift each envelope to its *S*-wave arrival (after normalizing for its maximum) and stack the traces at each station in order to form an average envelope-per-station (array envelope). Each transverse envelope calculated at different stations (Figs 1 and 2) is the average of those produced by the earthquakes in the cubic region marked by X, where the hypocentres are located between 1 and 2 km depth. The most important velocity anomaly in this depth range is the signature of the caldera rim (e.g. Battaglia *et al.* 2008). We show the trace of the caldera rim at 1.5 km depth as a broad grey circumference. Before dealing with the theory and the corresponding synthetics, we discuss the data envelopes in the whole caldera, both to remark non-uniform lateral scattering and to get a better insight into the scattering propagation at different distances.

Downloaded from http://gji.oxfordjournals.org/ at University of Edinburgh on Decem

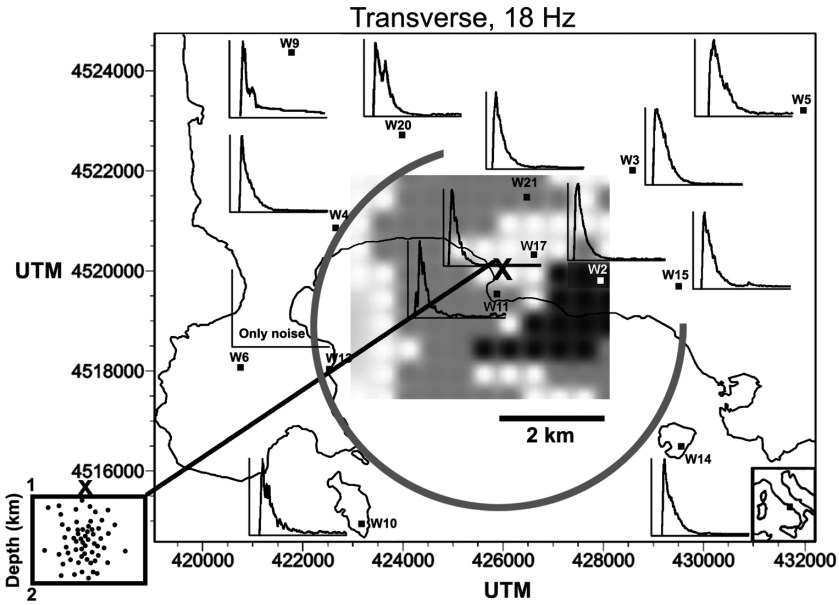

Figure 1. The transverse rms *S*-wave array envelopes normalized for their maximum values are obtained at 11 stations (black squares) located at Campi Flegrei caldera (map) in the 18 Hz frequency band. A **X** marks the epicentre zone (a cube of 1 km side, centred at 1.5 km depth). The earthquakes span depths between 1 and 2 km. The timescale for each envelope is 30 s. The results of the separation of intrinsic versus scattering attenuation performed by De Siena *et al.* (2011) is superimposed on the centre of the caldera. Light grey represents dominant scattering attenuation while black represents dominant intrinsic attenuation, respectively. The broad dark-grey circumference marks the inner contour of the annular caldera rim at 1.5 km depth, and is deduced by using the velocity tomographic images of Battaglia *et al.* (2008).

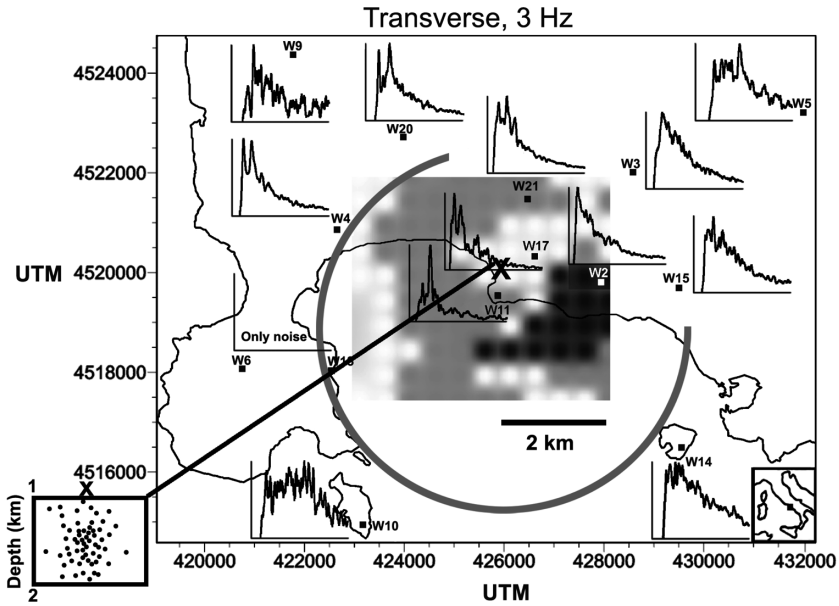

Figure 2. Same as Fig. 1 for the 3 Hz frequency band.

In order to model the recorded envelopes with a 2-D simulation we will constrain our interpretation to the first 3 km depth in an area of lateral dimension $L = 10$ km.

2.1 Envelopes at 18 Hz

In Fig. 1, we show the transverse normalized *S*-wave envelope recorded at each station after filtering in the 18 Hz frequency band with a bandwidth of 6 Hz. In this frequency band we expect strong forward *SS* scattering producing a relatively high and thin peak for the *S*-direct arrival (t_S) with a smooth exponential decrease at larger lapse times (Del Pezzo 2008). We also expect the degree of anisotropic scattering to be higher at 18 Hz than at 3 Hz, even if, due to the large number of collisions, the effect of anisotropic scattering will quickly be lost (Yamamoto & Sato 2010).

Most of the stations in the caldera present a clear increase in the envelope amplitude due to the arrival of the direct *S* waves. This is followed in many cases by a second peak of relatively large intensity in the early coda (W21, W17, and, more evidently, W11 and W20). This high intensity is particularly evident on the transverse envelopes in the western and central quadrants (Fig. 1, e.g. station W20). Eastern stations present instead a larger broadening (e.g. compare W3 and W4). Going further away from the epicentre (e.g. stations W3) a diffusive-shaped broadened envelope is observed.

Downloaded from http://gji.oxfordjournals.org/ at University of Edinburgh on December 28, 2013

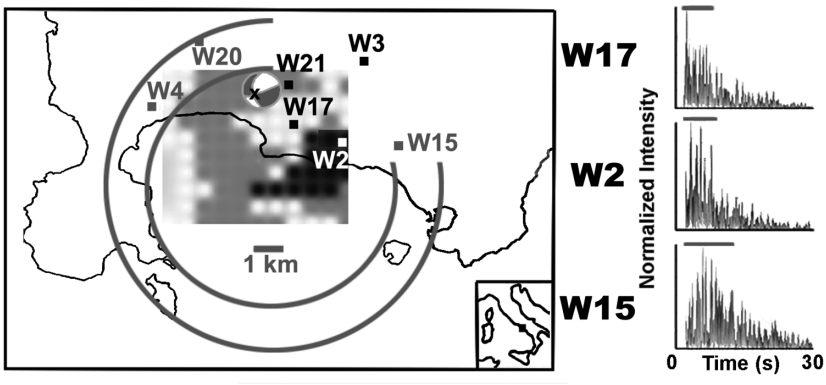

Figure 3. Map of the Campi Flegrei caldera with three unfiltered transverse intensity measurements recorded at stations W17, W2 and W15. The source frequency is 3 Hz, while the spectrum corner frequency is around 10 Hz. The epicentre is located at 1.5 km from the centre of the block (**X**) shown in Figs 1 and 2, left-hand lower panel. The grey broken annulus depicts the caldera rim at 1.5 km (see Fig. 1). In the lower-right-hand corner a black square shows the location of the Campi Flegrei caldera in Italy. We correct the direct intensities for the corresponding focal mechanism obtained by Zollo & Bernard (1991). The horizontal grey line on each of the envelopes shows the pulse broadening t_d as defined in Section 2.3.

In the 18 Hz frequency range the typical exponentially decreasing pattern of the coda envelope is rarely interrupted by large anomalous intensities, except in the area northwest of the epicentres (Fig. 1).

2.2 Envelopes at 3 Hz

In Fig. 2, we show the normalized transverse *S*-wave envelopes calculated in the 3 Hz frequency band with a bandwidth of 2 Hz. Most stations in proximity of the epicentral zone present a distinct direct peak (e.g. stations W17, W21 and mainly W2). This peak is usually followed by a second peak of equal (stations W4, W20 and W21) or larger (e.g. station W11) intensity in the central and western caldera. In the envelopes recorded north, west and south of the epicentres, and at distances smaller than 3 km, this distinctive peak characterizes early and intermediate coda envelopes; this common behaviour suggests that a similar scattering medium is sampled by the wavefields. The envelopes are broad in time everywhere, especially in the easternmost zones (stations W2, W3 and W15) where there is no evident intermediate coda peak. These observations agree with the scattering images obtained by De Siena *et al.* (2011) who find a dominant scattering attenuation in the western quadrant (light grey, Figs 1 and 2) with respect to a dominant intrinsic attenuation in the eastern quadrant (black, same figures). Hence, we expect an highly scattering body affecting the envelopes recorded in the western part of the caldera, which could enlarge envelopes in time and produce the observed anomalous coda envelope peak.

As the ray distance increases we observe anomalous multiple scattering (e.g. stations W4, W21 and W5) with delay in the exponential decrease, starting at times as large as eight times the *S*-wave direct arrival (t_S, station W5). The highest peak in this envelope is as late as 4 t_S and is hardly discernible from the early coda constant trend, which cannot be modelled by single scattering (Fig. 2). The recordings at station W9, on the northwestern side, have a completely different behaviour in the two frequency bands and with respect to station W5. A high direct *S*-wave peak characterizes the envelope at 18 Hz while at 3 Hz the envelopes present a diffusive-like average behaviour with no amplitude decrease with increasing lapse time, and several anomalously high intensities in the intermediate and late coda. We assume that the effect of horizontal highly scattering interfaces does not affect our measures, if we constrain our earthquakes between 1 and 2 km depth. Especially at larger ray distances this assumption could be violated in both frequency bands.

2.3 Single earthquake intensity measurements

Multiple scattering effects in coda envelopes can be shown considering the propagation of the wavefield produced by a single earthquake, and recorded at three stations east of the epicentre (Fig. 3). The earthquake occurred on 1984 April 1, and the earthquake magnitude ($M = 2$) and source mechanism (shown in Fig. 3) were calculated by Zollo & Bernard (1991). Considering that the three stations are located at increasing distances on roughly the same azimuth of propagation, we assume that the differences in the envelopes are mainly caused by the medium, and not by the source radiation pattern. The seismograms are RTZ rotated and the *S*-wave traveltimes are computed by using the same ray-bending approach used for array analysis (Thurber & Eberhart–Phillips 1999; Levander & Nolet 2005).

With increasing distance, the scattered intensity quickly increases at the expense of the direct intensity, and the maximum intensity is observable at larger lapse times. The envelopes are clearly affected by multiple scattering, with a large number of high amplitude peaks in the early and intermediate coda (stations W17 and W2). These could be related to several deterministic high scattering centres, with the randomness of the interaction averaged out by the large number of scattering events. To measure the strength of these effects we define the envelope duration t_d as the lag time between the *S*-wave onset and the time when the transverse rms decays to half its maximum amplitude (Saito *et al.* 2005). t_d is shown in Fig. 3 as a horizontal broad grey segment above each envelope, and it is of the same order as t_S. Filtering at 18 Hz produces more compact envelopes (Fig. 1): t_d is usually less than the *S*-wave traveltime in this frequency band, while this rarely happens at 3 Hz.

At the nearest two stations a drastic intensity decrease characterizes both envelopes after a few seconds. At station W15 the envelope does not show this steep decrease, and presents instead a diffusive behaviour, with a smooth late coda envelope decrease. The complexity in the envelope-decay model is directly responsible for the difficulties found in imaging attenuation and scattering at frequencies lower than 6 Hz across the caldera (Tramelli *et al.* 2006; De Siena *et al.* 2010). In the next section, we try to model the envelopes with a homogeneous Monte Carlo multiple scattering simulation with single scattering anisotropic coefficients (Gusev & Abubakirov 1996). From the diffusive shape of the coda envelopes at relatively small distances (see e.g. the envelope at station W15 in Fig. 3) and from the results obtained by Tramelli *et al.* (2006)

Downloaded from http://gji.oxfordjournals.org/ at University of Edinburgh on Decem

we will then propose the presence of a reflective diffusive boundary, which affects the coda envelope behaviour in different ways at different frequencies. Hence, we assume that a laterally non-homogeneous scattering medium can model real envelopes better than a homogeneous scattering medium, and that the understanding the complex effects induced by a non-uniformly scattering medium is of importance to obtain a reliable model of scattering propagation.

3 MONTE CARLO SIMULATION OF MULTIPLE SCATTERING WAVE PROPAGATION

Multiple scattering theory describes wave propagation for a random distribution of scatterers via multiple sequential single scattering approximations. The single scattering coefficients provide the scattering pattern at each scattering event and multiple single scattering events produce the entire coda envelope. We start with a multiple scattering model, hence, we solve the radiative transfer equations using the Monte Carlo method in the fully elastic case (Margerin *et al.* 2000; Przybilla *et al.* 2006; Yamamoto & Sato 2010).

3.1 Statistical description of the medium

A statistical description of the medium through its correlation and spectral properties is necessary in order to model scattering propagation (Rytov *et al.* 1987). We consider a crustal area of average dimension $L = 10$ km, which can be described as an ensemble of random media, and characterized by a 2-D random velocity field (Fig. 4). In our particular hypocentral configuration wave propagation is mostly contained in the first 3 km depth at Campi Flegrei, above the drastic horizontal change of velocity and attenuation imaged by several tomography studies (e.g. Zollo *et al.* 2008). This field $V(\vec{x})$ is described in terms of the average wave velocity V_0 and the fractional velocity fluctuation $\xi(\mathbf{x})$, where $\mathbf{x}$ is the 2-D space coordinate (Sato & Fehler 1998)

$$V(\mathbf{x}) = V_0\{1 + \xi(\mathbf{x})\}. \quad (1)$$

We define $R(\mathbf{x})$, the autocorrelation function (ACF) of the fractional velocity fluctuations between points of positions $\mathbf{x}$ and $\mathbf{x}'$, as

$$R(\mathbf{x}) \equiv \langle \xi(\mathbf{x} + \mathbf{x}')\xi(\mathbf{x}') \rangle, \quad (2)$$

and its Fourier transform, the power spectral density function (PSDF, Ψ) as

$$\Psi(\mathbf{k}) = \int_{-\infty}^{\infty} R(\mathbf{x}) \exp(-i\mathbf{k}\mathbf{x}) d\mathbf{x}, \quad (3)$$

where $\mathbf{k}$ is the wavenumber, and angular brackets stand for ensemble averaging. The PSDF is the key function to describe the scattering properties of the medium and its form must be chosen in order to represent real coda envelopes.

A power-law PSDF corresponds to an exponential or, more generally, a von Kármán-type ACF (Shapiro & Hubral 1999). The von Kármán PSDF is given as

$$\Psi(\mathbf{k}) = \frac{4\pi\epsilon^2 a^2 \kappa}{(1 + a^2\mathbf{k}^2)^{(\kappa+1)}}, k > 0, \quad (4)$$

where a is the correlation length, $\epsilon^2 \equiv R(0) = \langle \xi(\mathbf{x})^2 \rangle$ is the mean square of the velocity fluctuations, and κ is the order of the function, which controls the decay of the PSDF.

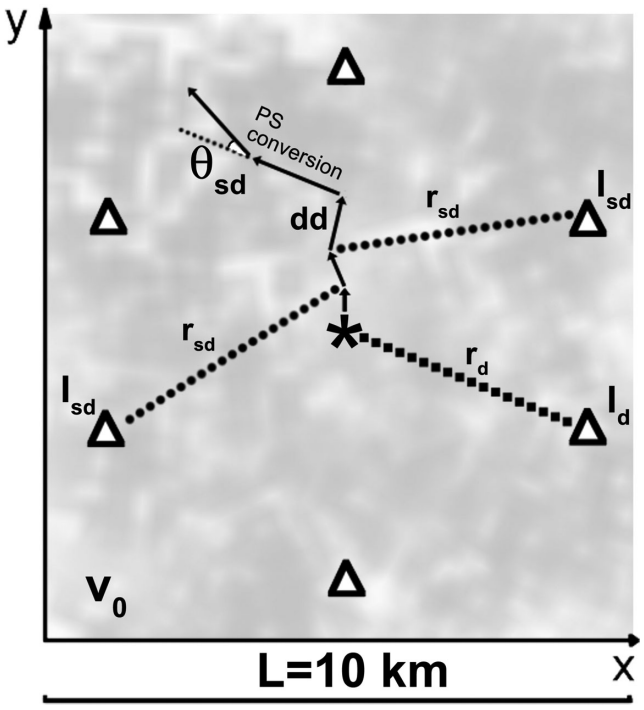

Figure 4. Sketch of the single scattering simulation for a source emitting P waves (star) in a square of $L = 10$ km side. The source produces a direct intensity (I_d) recorded at distance r_d (dashed line). After each step of the simulation (*dd*, controlled by the mean free paths) the scattered intensity (I_{sd}) is recorded at every station (triangles) each at distance r_{sd} (dotted lines). The medium is characterized by its average velocity V_0 and its fractional velocity fluctuations ξ (light grey background medium). The scattered intensity is dependent both on the scattering angle (θ_{sd}) and on the scatterer-receiver distance r_{sd}. In case of *PS* (or *SP*) conversion the particle deviates strongly from its incidence direction.

In seismology, an exponential PSDF has been shown to be preferable to a Gaussian one in order to better predict seismic envelopes (Shiomi *et al.* 1997; Sato & Fehler 1998; Przybilla *et al.* 2006). In a volcanic medium we assume that short-wavelength spectra dominate with respect to long-wavelength ones, causing anomalous broadening of the envelopes in time and quick loss of coherence for the direct waves. Multiple scattering simulations with single scattering coefficients and with an exponential ($\kappa = 0.5$) ACF provide envelopes at regional distances, which are similar to the recorded envelopes, and we assume this value in the following sections.

The scattering coefficients depend on the typical correlation distance for a volcanic area (a). Holliger & Levander (1992) found an average correlation length for the continental crust between 0.2 and 0.8 km. ACF velocity measurements at Campi Flegrei provide a value of $a = 0.9$ km (De Siena *et al.* 2011) for the first 4 km of the crust, as well as an elevated mean squared fluctuation of $\epsilon^2 = 6$ per cent. It is well known that, decreasing the correlation length, the probability of conversion increases, while anisotropy decreases (Sato *et al.* 2004; Przybilla *et al.* 2006). A smaller correlation length can also account for the complexities in the *S*-wave velocity field between 0 and 3 km depth, and can better characterize the heterogeneous volcanic medium for both direct waves (De Siena *et al.* 2010). Yoshimoto *et al.* (1997) discuss several possible values of a and ϵ in volcanic environment, in order to obtain the three component seismic envelopes in the 8–16 Hz frequency band, finding that a correlation length lower than 0.5 km matches observations. In our first description of the medium (see Tables 1 and 2) we lower

Downloaded from http://gji.oxfordjournals.org/ at University of Edinburgh on December 28, 2013

Table 1. Single total scattering coefficients at two different frequencies, for the propagation medium with $\epsilon^2 = 0.01$ and $a = 0.1$ km.

	km^{-1}	3 Hz	18 Hz
$\kappa = 0.5$	g^0_{ss}	0.023	0.876
	g^0_{pp}	0.005	0.176
	g^0_{ps}	0.009	0.035
	g^0_{sp}	0.004	0.015

Table 2. Mean free paths, transport mean free paths and diffusion constant for $\kappa = 0.5$ and for the propagation medium with $\epsilon^2 = 0.01$ and $a = 0.1$ km.

km	3 Hz	18 Hz
l_p	71.58	4.74
l_s	36.84	1.12
l^*_p	129.63	30.81
l^*_s	86.59	24.12
D	121.65	31.57

a to 0.1 km. This value, together with $\epsilon = 10$ per cent and with an exponential ACF, provides scattering quality factors similar to the ones calculated at Campi Flegrei [for a complete review, we refer to Del Pezzo & Bianco (2013)].

In our second description we consider a higher a value (1 km) like the one proposed by De Siena *et al.* (2011) or Yamamoto & Sato (2010). This produces smaller mean free paths (see Tables 3 and 4) hence, a larger number of interactions. In Section 3.5, we will select the best a value comparing the result of our simulations with the most regular of our envelopes, obtained at station W2. The mean free paths can also decrease with the increase of ϵ^2, producing a larger number of interactions. However, a larger ϵ^2 would produce effects on both the direct and the scattered wavefields, which cannot be seen in our data. Hence, $\epsilon = 10$ per cent remains constant through our analysis.

Table 3. Single total scattering coefficients at two different frequencies, for the propagation medium with $\epsilon^2 = 0.01$ and $a = 1$ km.

	km^{-1}	3 Hz	18 Hz
$\kappa = 0.5$	g^0_{ss}	0.261	10.129
	g^0_{pp}	0.051	1.951
	g^0_{ps}	0.004	0.004
	g^0_{sp}	0.002	0.001

Table 4. Mean free paths, transport mean free paths and diffusion constant for $\kappa = 0.5$ and for the propagation medium with $\epsilon^2 = 0.01$ and $a = 1$ km.

km	3 Hz	18 Hz
l_p	18.15	0.51
l_s	3.80	0.10
l^*_p	244.90	135.76
l^*_s	187.81	95.30
D	248.00	130.87

3.2 Single scattering coefficients

We simulate the multiple scattering wavefield by shooting particles from a point source located in the caldera, whose velocity field is statistically characterized by a von Kármán PSDF. Collisions of the particles with each scatterer are perfectly elastic. The scattered direction, chosen randomly with a table look-up method, is governed by the differential single scattering coefficients (Przybilla *et al.* 2006).

The differential single scattering coefficients are dependent on the von Kármán PSDF Ψ as well as on the scattering patterns, $|X_{ij}(\theta)|^2$. Here θ is the angle with respect to the incident direction (Fig. 4) while i and j each stand for either P or S (Sato & Fehler 1998). The SS differential scattering coefficient g_{ss} is given by

$$g_{ss}(\theta) = \frac{k_s^3}{8\pi}\Psi\left[2k_s \sin\left(\frac{\theta}{2}\right)\right]|X_{ss}(\theta)|^2, \tag{5}$$

where k_s is the S wavenumber, density is correlated to velocity by the factor $\nu = 0.8$ (given by Birch's law) and $X_{ss}(\theta)$ is defined by

$$X_{ss}(\theta) = [\nu(\cos\theta - \cos 2\theta) - 2\cos 2\theta]. \tag{6}$$

SS scattering dominates for large lapse times in the continental lithosphere—for a complete review on the variations of the scattering coefficients with space, time and frequency (see Sato *et al.* 2012). In this paper, we refer to the 2-D equivalent of the differential scattering coefficients, extensively treated by Przybilla *et al.* (2006).

P- and S-wave mean free paths (l_p and l_s, respectively) are the average distances travelled by a particle between two collisions, and are dependent on the single scattering coefficients

$$g^0_{ij} = \frac{1}{2\pi}\int_0^{2\pi} g_{ij}(\theta)\,\mathrm{d}\theta. \tag{7}$$

We introduce the notation

$$g^0_p = g^0_{pp} + g^0_{ps} \tag{8a}$$

$$g^0_s = g^0_{sp} + g^0_{ss}, \tag{8b}$$

where the cross-terms satisfy the 2-D reciprocity relation

$$g^0_{ps} = \left(\frac{V_p}{V_s}\right) g^0_{sp}, \tag{9}$$

and V_p and V_s are P- and S-wave velocities. Hence, the mean free paths are

$$l_p = (g^0_p)^{-1} \tag{10a}$$

$$l_s = (g^0_s)^{-1}. \tag{10b}$$

The single total scattering coefficients numerically calculated for 3 and 18 Hz are shown in Tables 1 and 3 for $a = 0.1$ and 1 km, respectively. We also numerically compute the scattering pattern associated with each scattering mode to select the direction after each scattering event (θ_{sd} in Fig. 4) with a table look-up method. At 3 Hz PS- and SP-conversion probabilities are almost as strong as the probability of SS-scattering. The associated single scattering pattern is only slightly anisotropic; in volcanic regions, multiple scattering at large lapse times is considered as isotropic, even if each scattering process is not (Yamamoto & Sato 2010). With evidence of multiple scattering this approximation would seem viable in this lower frequency band. At 18 Hz, even if the probabilities of conversion scattering are still finite, they are much lower than the SS-scattering probability (Tables 1 and 3). The increase of a produces lower conversion probabilities (g^0_{sp}, Table 3) and higher

Downloaded from http://gji.oxfordjournals.org/ at University of Edinburgh on Decem

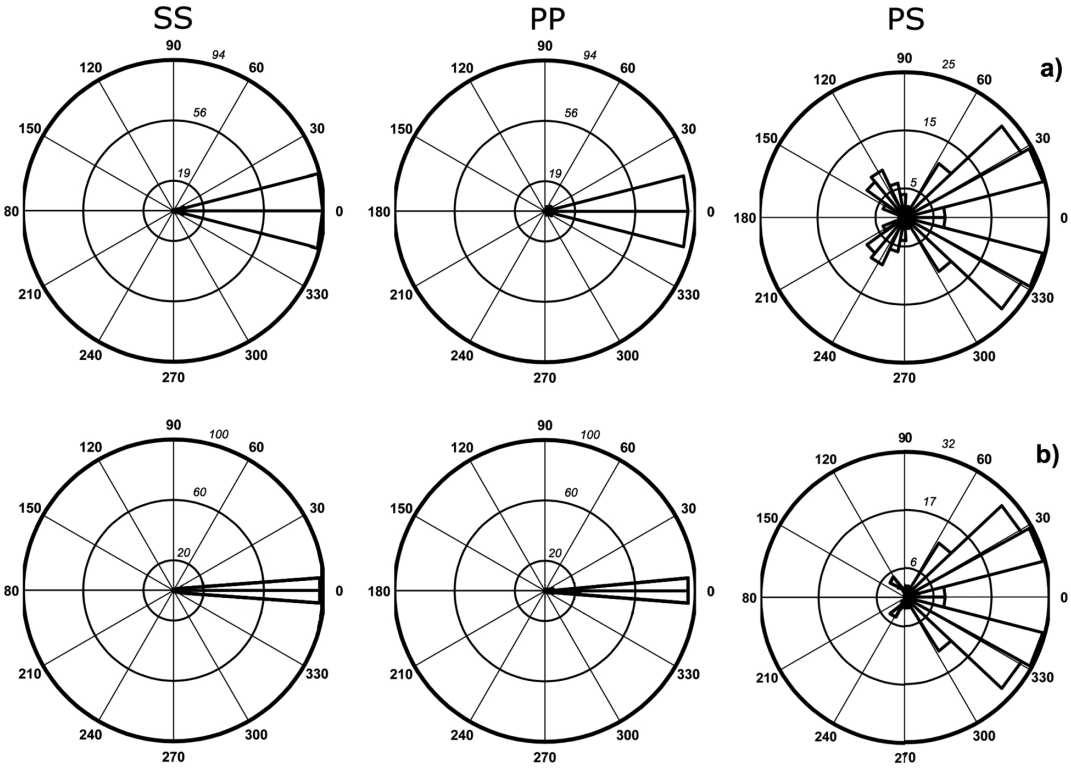

Figure 5. (a) Histograms representing the scattering pattern for *SS* (first) *PP* (second) and *PS* (third) scattering at 18 Hz for $a = 0.1$ km (Table 1). We produce 201 random angles with the probability defined by the differential scattering coefficients, and add each of them to the corresponding interval (in degrees). The angle is with respect to the incident direction, which is always zero. (b) Histograms for $a = 1$ km (Table 3).

anisotropy (compare Figs 5a and b) which reduce the advantage of having a shorter mean free path (Sato *et al.* 2004).

Different single scattering patterns characterise *PP*-, *SS*- and *PS*-scattering (scattering modes). We create tables including 201 angles, each angle corresponding to an equal fraction of the total cross-section, given by the integral over 2π of the scattering coefficients (eq. 5). Direction is selected by using a random integer number (defined between 1 and 201): from the scattering pattern (Figs 5a and b) it is evident that scattering is most likely in the forward direction for *SS* and *PP* scattering, while the *PS* (and *SP*) scattering patterns present different preferential directions. Conversion scattering induces a relevant deviation from the incident direction, causing a larger sampling of the medium (e.g. Fig. 4).

3.3 Transport mean free path and diffusion

Instead of single scattering coefficients, some authors prefer to simulate envelopes at large lapse times excluding strong forward scattering from the anisotropic single scattering coefficients (Sato *et al.* 2004). This can be done including the factor $(1 - \cos\theta)$ in the definition of g_{ij} (Gusev & Abubakirov 1996; Sato *et al.* 2004). The *SS* differential momentum transfer scattering coefficients (g^m_{ss}) are therefore defined using eq. (5)

$$g^m_{ss}(\theta) = (1 - \cos\theta)\frac{k_S^3}{8\pi}\Psi\left(2k_s \sin\frac{\theta}{2}\right)|X_{ss}(\theta)|^2. \tag{11}$$

Nevertheless, it is known since the works of Weaver (1990) and Ryzhik *et al.* (1996) that the equivalent scale lengths (the transport mean free paths) have more complicated expressions than those obtained from momentum transfer scattering coefficients, at least in the full elastic case. Therefore, we introduce the cosine weighted

Table 5. Cosine weighted scattering coefficients at two different frequencies, for the medium with $\epsilon^2 = 0.01$ and $a = 0.1$ km.

	km^{-1}	3 Hz	18 Hz
$\kappa = 0.5$	g^*_{ss}	0.013	0.839
	g^*_{pp}	0.003	0.162
	g^*_{ps}	0.004	0.020
	g^*_{sp}	0.002	0.009

scattering coefficient for the various mode conversions g^*_{ij} (Table 5) as

$$g^*_{ij} = \frac{1}{2\pi}\int_0^{2\pi} g_{ij}(\theta)\cos\theta \mathrm{d}\theta, \tag{12}$$

where g_{ij} are the single scattering coefficients. Using these expressions, we obtain the transport mean free paths (l^*_p and l^*_s, Table 2) in the fully elastic case (Turner 1998)

$$l^*_p = \frac{g^0_s - g^*_{ss} + g^*_{ps}}{(g^0_p - g^*_{pp})(g^0_s - g^*_{ss}) - g^*_{ps}g^*_{sp}} \tag{13a}$$

$$l^*_s = \frac{g^0_p - g^*_{pp} + g^*_{sp}}{(g^0_p - g^*_{pp})(g^0_s - g^*_{ss}) - g^*_{ps}g^*_{sp}}. \tag{13b}$$

In the case of non-preferential scattering (i.e. equal amounts of forward and backward scattering) the transport mean free paths reduce to the mean free paths. It should be noted that no well-defined transport mean free path exists in the case of coupled elastic waves: the transport mean free path of *P* and *S* waves cannot effectively be measured separately.

Downloaded from http://gji.oxfordjournals.org/ at University of Edinburgh on December 28, 2013

Diffusion represents the scattering radiation field at large lapse times from the source nucleation time. It assumes an energy flux scattered in space almost uniformly in every direction, recorded after encountering many particles. A slightly anisotropic angular dependence (like the one obtained from cosine weighted scattering coefficients) is necessary to add net power propagation, still present in the diffusion regime. Nevertheless, in the diffusion approximation, the diffuse intensity $I_{\rm D}$ can be expanded into the first two terms of its Taylor expansion in the directional component only (Akkermans & Montambaux 2007, pp. 170–172). The specific intensity corresponding to this approximation in the 2-D case at distance r can be written as the sum of the average diffuse intensity $[I_{\rm D}(r)]$ and a term containing the scalar product of the current associated with the specific intensity $[\overline{J}_{\rm D}(r)]$ for a unit vector $\hat{s}$ as

$$I_{\rm D}(\vec{r},\hat{s}) = I_{\rm D}(\vec{r}) + \frac{1}{\pi}\overline{J}_{\rm D}(\vec{r})\cdot\hat{s}. \tag{14}$$

For diffusion to be valid, the second term must be much smaller than the first.

The diffusion constant (or diffusivity, D, Table 2) is the sole quantity controlling diffuse energy density $[E_D(r,t)]$ at distance r in the case of 2-D propagation

$$E_D(r,t) = \frac{\exp\left(-\frac{r_d^2}{4Dt}\right)}{4\pi Dt}, \tag{15}$$

where r_d is the source–station distance and t is the time. As in 3-D, diffusion of P and S waves in 2-D requires equipartition to be reached (Hennino *et al.* 2001; Margerin 2006)

$$\frac{E_s}{E_p} = \frac{V_p^2}{V_s^2}, \tag{16}$$

where E_p and E_s are the energies for P and S waves. Note that in 2-D P waves can only couple with SV waves. Hence, from the expression of the diffusivity of elastic waves in 3-D given by eq. (5.46) of Ryzhik *et al.* (1996, p. 54) we deduce the following 2-D diffusivity:

$$D = \frac{1}{1+\gamma^2}\left(\frac{V_p l_p^*}{2} + \frac{\gamma^2 V_s l_s^*}{2}\right), \tag{17}$$

where $\gamma = \frac{V_p}{V_s}$. The diffusivity, the mean free paths, and the transport mean free paths are reported in Tables 2 and 4 for different frequencies in the two cases ($a = 0.1$ and 1 km).

3.4 Synthetic envelopes in a statistically homogeneous medium

We follow a 2-D scattering scheme valid for both P and S waves, similar to those of Przybilla *et al.* (2006); for P waves, propagation is depicted in Fig. 4. We assume a volcano-tectonic Ricker point source located near the centre of the caldera, emitting most of its energy around 3 Hz, with 10 per cent of the energy emitted in the 18 Hz frequency band (Chouet 2003). The impulsive source radiates totally coherent P- and S-wave energies at $t = t^0$, where t^0 is the nucleation time, with energy ratio $E_p/E_s = \frac{1}{23}$.

The coherent intensities at time t $[I_{p,s}(t)]$ propagate in the homogeneous medium of velocity V_0 (which can be P- or S-wave velocity). They are produced by an isotropic source at time t_0 and recorded at a receiver-distance R at the P- and S-wave arrival times $(t_{p,s})$

$$I_{p,s}(t) = \frac{1}{2\pi R}\delta\left(t - t^0 - \frac{R}{V_0}\right)\exp\left(-\frac{R}{l_{p,s}}\right). \tag{18}$$

The receiver distance R is the distance travelled by the coherent (or mean) wavefield, and mainly corresponds to the intensities in a time window around the seismic primaries. t_0 is the enucleation time, while δ stands for delta function. We assume this as a valid approximation, that is, that the tails of the 2-D Green's function in the scattering medium produce only second order effects on our envelopes (Paasschens 1997). To account for the real source shape we apply a convolution operator [$Ri(t,f)$, dependent on time t and frequency f and corresponding to a 3 Hz Ricker wavelet] to the whole envelope in the frequency space (Ryan 1994). The form of this convolution operator in the time–space is

$$Ri(t,f) = (1 - 2\pi f^2 t^2)\exp(-\pi^2 f^2 t^2) \tag{19}$$

with breadth [$B(f)$, the time interval between the centre of each of its two characteristics side lobes]

$$B(f) = \frac{\sqrt{(6)}}{\pi f} = 0.26\,s. \tag{20}$$

This convolution represents the source time-function effect on the Monte Carlo solutions at every lapse time.

We simulate the length of a random walk dependent on the mean free paths as Przybilla *et al.* (2006). The distance between collisions (dd, Fig. 4) is

$$dd = -l_{p,s}\ln(\alpha), \tag{21}$$

where α is uniformly distributed between 0 and 1. The (eventual) change in polarization and the direction after scattering are controlled by the single scattering coefficients and the relative scattering patterns (Table 1 and 3 and Figs 5a and b). The scattering coefficients are a direct measure of the probability of *PP, SS, PS* or *SP* scattering (Przybilla *et al.* 2006). A random number defines the polarization, a second one determines the direction after scattering (angle θ in Fig. 4) using the tables.

After each collision, the intensity scattered at a receiver at distance $r_{\rm sd}$ ($I_{\rm sd}$) is recorded by using the joint probability of detecting a particle of given polarization (Margerin *et al.* 2000)

$$I_{\rm sd} = \Upsilon(i,j,a,k,\theta_{\rm sd},\kappa)\frac{\exp\left(-\frac{r_{\rm sd}}{l_{p,s}}\right)}{r_{\rm sd}}. \tag{22}$$

The probability Υ is dependent on the recorded and incident mode i, j (*PP, SS ,PS* or *SP*) on $\theta_{\rm sd}$ (the angle between the propagation direction and the scatterer–receiver direction) and on the order of the von Kármán function ($\kappa = 0.5$). The dependency of Υ on $\theta_{\rm sd}$ expresses the intrinsic forward anisotropy of the problem: if a particle is shot towards east at 18 Hz the receivers in the eastern part record intensities much higher than those in the western part, since it is extremely unlikely that the particle scatters backwards.

The total number of propagated particles in every simulation of this paper is $N = 10^6$. The simulation is repeated for a number of sources equivalent to the one considered in the data. The location of the sources varies randomly in a square of 1-km-side length, to account for the different hypocentres in the real data. The final image is the average of the intensities produced by the different sources. The code is parallelized using OpenMP (for the detection at different receivers) and MPI (for the simulation at different sources). This is of extreme importance at 18 Hz, due to the reduced S-wave mean free path (e.g. Table 4) producing a large number of collisions.

At $L = 10$ km we include a radiative transfer boundary condition (Akkermans & Montambaux 2007, p. 156). The probability in eq. (22) vanishes in such a way that a particle which leaves the system never returns. We also shoot energy corresponding to 1 per cent

Downloaded from http://gji.oxfordjournals.org/ at University of Edinburgh on Decem

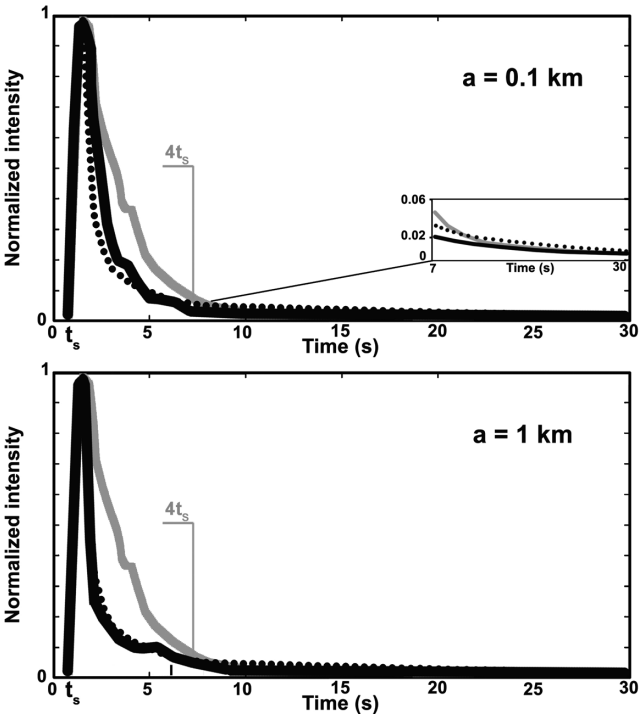

Figure 6. Transverse normalized array envelopes (bold grey lines) calculated at station W2 in the 18 Hz frequency band. Top panel: the array envelopes are compared with the corresponding synthetics (bold black lines) and with the diffusion solutions for an exponential medium of order $\kappa = 0.5$ (dotted line) for the model with $\epsilon^2 = 0.01$ and $a = 0.1$ km, corresponding to Tables 1 and 2. The times at which the array envelopes coincide with the diffusion solutions are 8 s (four times t_s) at 18 Hz and 16 s (four times t_s) at 3 Hz. The behavior of the three curves is shown in the insert, for the time interval 7–30 s. Bottom: The same comparison for the model with $\epsilon^2 = 0.01$ and $a = 1$ km, corresponding to Tables 3 and 4.

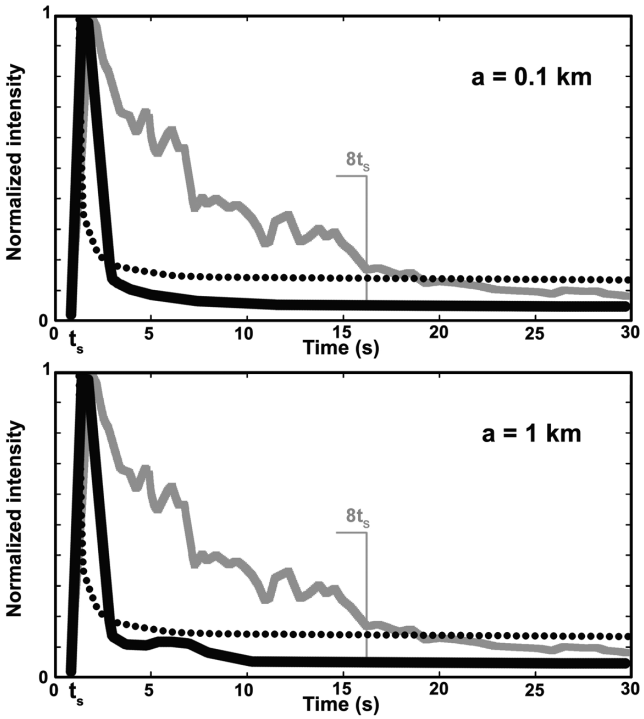

Figure 7. Same as Fig. 6 in the 3 Hz frequency band.

of the intensity produced by the earthquake from this boundary, choosing the shooting point randomly on the square of Fig. 4. The corresponding intensities simulate noise produced outside of the region, and are only relevant in the synthetics at 3 Hz (Figs 6b–8b).

3.5 Envelopes at 1.6 and 3.8 km transverse distance

We consider the array envelopes obtained after filtering in the 18 and 3 Hz frequency bands, recorded at 1.6 km transverse distance (Figs 6 and 7, bold grey lines). The corresponding station is labelled as W2 in Figs 1 and 2; we remark that this is not the station nearest the epicentre (marked as **X** in the centre of the caldera, North of Pozzuoli) but the corresponding array envelope is almost devoid of anomalous high late coda intensities. The solid black lines in Figs 6 and 7 show the synthetic intensities obtained for a single source and $\kappa = 0.5$. We also compare the Monte Carlo solutions at both frequencies with the diffuse intensities (dotted lines, Figs 6 and 7) given by eq. (15) using the diffusivity D given by Tables 2 and 4.

At both frequencies the synthetic and the array envelopes are in good agreement for the first part of the envelope, after averaging over many sources in the 1 km cube (Figs 6 and 7) while the intermediate coda intensities are more than twice the synthetic ones. The variable source location cannot model the ratio between the early and the late coda intensities or the phases of the anomalous intermediate coda intensities, almost absent in the synthetics. Even after many collisions, the anisotropy for the case $a = 1$ km diminishes only slightly, and the simulation with $a = 0.1$ km better

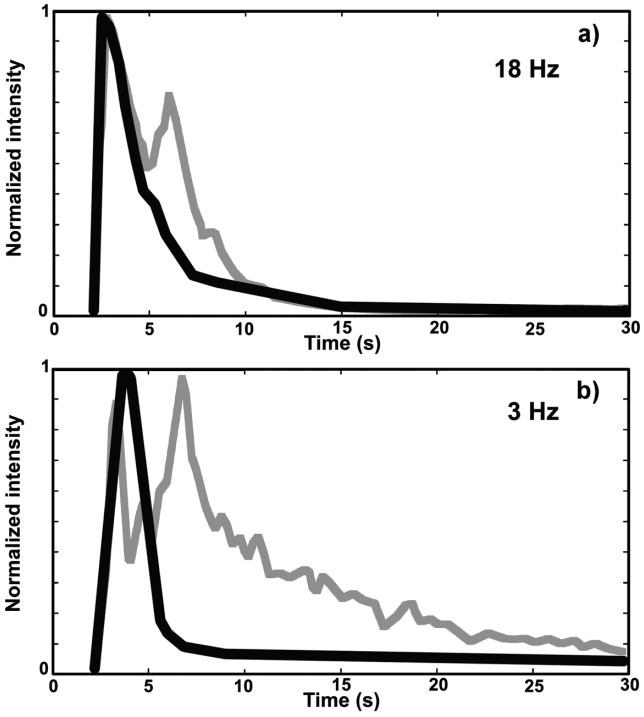

Figure 8. Transverse normalized array envelopes (bold grey lines) calculated at station W20 in the 18 Hz (a) and 3 Hz (b) frequency bands. The array envelopes are compared with the corresponding synthetics (bold black lines) for the model with $\kappa = 0.5$, $\epsilon^2 = 0.01$ and $a = 0.1$ km, corresponding to Tables 1 and 2.

fits coda envelope durations at 18 Hz (Figs 6a and b). After approximately 4 t_S (8 s, 18 Hz) and 8 t_S (16 s, 3 Hz) the diffusion intensities cross the array envelope intensities. This is not a strong constraint for the reach of the diffusion regime in the caldera after

Downloaded from http://gji.oxfordjournals.org/ at University of Edinburgh on December 28, 2013

this time limit. Nevertheless, it suggests that the lapse time required for the application of diffusive techniques (e.g. coda-wave interferometry) in such a complex medium could be as large as the ones usually assumed in volcanic cones. For a discussion on the lapse time required to reach the equipartition state in volcanoes using active data see e.g. Yamamoto & Sato (2010). This is a problematic issue when considering poor quality passive data. A clear difference between synthetic and diffusion solutions can be seen after 8 t_S at 3 Hz, while this is not so evident at 18 Hz (Fig. 6a, small panel).

We interpret these results as due to the difference in the scattering regime between the two frequency bands, or to the inapplicability of the current theory to the 3 Hz frequency range. At 3 Hz, a mean free path like the one obtained for $a = 0.1$ km does not produce variations, and only the direct S wave can be observed. However, even lowering the mean free path with $a = 1$ km, observations are not matched (Fig. 7). The increase of the coda level after 5 s does not justify the use of a larger correlation length. The product of the P (or S) wavenumber ($k_{p,\,s} = k$) and the correlation length a is always larger than 1 at 18 Hz ($k_s a = 7.5$ and $k_s a = 75$ with $a = 0.1$ km and $a = 1$ km, respectively). In the 3 Hz frequency band, it is not the case for the lower correlation length ($k_s a = 1.2$ and $k_s a = 12$ with $a = 0.1$ and $a = 1$ km, respectively). This is a clear indication that more complex effects than the ones considered could affect the 3 Hz scattered wavefield.

These differences between data and synthetics may be ascribed to the 3-D nature of scattering in the area, as derived by scattering and attenuation tomography (Tramelli *et al.* 2006; De Siena *et al.* 2010). However, we chose earthquakes vertically located between 1 and 2 km trying to image scattering propagation at best in the 2-D horizontal section at 1.5 km depth. At such short distances wave propagation is mainly constrained above the main horizontal velocity change, and we assume that the main changes in the scattering texture are vertical.

The time threshold at which diffusion is reached in real seismic data is dependent on topography, but in this study we concentrate on an area almost devoid of it. If compared with volcanic cones, where topography-effects may induce a quicker reach of diffusion or produce coda-localization effects, the synthetic envelopes could present larger differences with respect to the recorded envelopes (Aki & Ferrazzini 2000; Neuberg & Pointer 2000; Wegler 2003). We also assume that, relative to scattering, absorption is low (Margerin *et al.* 2001); this is not necessarily true in volcanic areas, even if intrinsic losses due to the presence of fluids and/or melt are considered of lower importance (e.g. Del Pezzo 2008). Since intrinsic absorption reduces the duration of the envelope we do not consider this parameter at present, and its effects will be discussed in the following sections.

The observations reported so far attest that a forward Monte Carlo model with the chosen statistical parameters ($a = 1$ km or $a = 0.1$ km, $\epsilon = 10$ per cent and $\nu = 0.8$) cannot provide an adequate model for the most regular of the envelopes in our data set, especially at 3 Hz. However, we cannot exclude to obtain a good fit of the envelope with a complete inversion of the same parameters. As an example, $\nu = 0.8$, the typical linear coefficient connecting density and velocity fluctuations for the lithosphere (Sato *et al.* 2012, chapter 4) could be too low for a volcanic area. Even if an increase of this parameter systematically increases backward scattering, a reasonable change did not provide strong changes of the envelope width. The two parameters tuning the coda envelope broadening and the absolute intensity are a and ϵ, in the current representation.

A decrease of the correlation length produces new preferential scattering directions (Sato *et al.* 2004) however the images of Tramelli *et al.* (2006) also justify this change only in a circular region centred on the middle of the caldera. As final proof that a homogeneous scattering model cannot model envelope broadening in the whole caldera, we show the result of our modelling for station W20, at a distance of 3.8 km from the epicentre area (Fig. 8). It is evident that the high coda intensities after the first arrival cannot be modelled by any inversion of the statistical parameters, since this would only produce a larger envelope, and not the occurrence of a second large intensity above the exponentially decreasing coda decay. Following Tramelli *et al.* (2006) we could decrease a in the diffusively scattering rim, designed on the one revealed by scattering tomography. The decrease of this parameter in a given region can strongly increase incoherent intensities, producing broad peaks at larger lapse times, but the range of ka is in this case results much less than one, excluding the application of radiative transfer theory with the used parameters.

A better explanation could be a sufficient increase of ϵ, producing both a decrease of the mean free path and of the transport mean free path, whose consequence is a larger number of interactions (e.g. Yamamoto & Sato 2010). Nevertheless, the scattering pattern of the single scattering collision is not strongly influenced by ϵ. Velocity fluctuations producing an $\epsilon > 10$ per cent for the whole area have not been revealed by the velocity tomography images (e.g. Battaglia *et al.* 2008). In Battaglia *et al.* (2008, fig. 13), the only sufficient velocity change in our depth range is shown for a semicircular area where velocity drastically changes (this area is interpreted as the signature of the caldera rim). We do not exclude that the results obtained by De Siena *et al.* (2011) and the intensity peaks in the coda may be due to a local increase of ϵ, since this does not contradict the importance of considering a non-uniformly scattering medium in order to model coda envelopes. Yet it is still possible to derive a transport equation with strong scatterers going beyond the Born approximation (Margerin 2013).

4 REFLECTIVE DIFFUSIVE SCATTERING: CHANGES IN THE SCATTERING TEXTURE

We propose the enhancement of the scattered intensities due to a change in the scattering texture as a feasible mechanism for modelling multiple scattering effects in the recorded coda envelopes (Turner 1998; Cormier & Li 2002; Monnereau *et al.* 2010). This inhomogeneity is more likely due to a local strong change of ϵ or a in the region of the caldera rim as suggested by Tramelli *et al.* (2006). We do not set new values of a and ϵ in this region, since a Monte Carlo simulation with these boundary conditions, even for the 2-D case, may be extremely complicated to implement, time consuming and incorrect, especially at 3 Hz (e.g. Binder & Heermann 2010, chapter 2). In our simplified model the caldera rim locally acts as a slab of randomly distributed scatterers, diffusively reflecting the incident intensities (Akkermans & Montambaux 2007, pp. 156–165).

We discuss the case of normal incidence of particles on a circular rim, its centre corresponding to the epicentre, wit radius $H = 3$ km. Fig. 9 shows the location of the four stations (A, B, C and D) for which we simulate the envelopes with respect to the rim. In the next section, we show the results of the inclusion of an annular rim in the original medium. This rim is characterized by both a different scattering texture (Fig. 9) and a finite thickness T. We

Downloaded from http://gji.oxfordjournals.org/ at University of Edinburgh on Decem

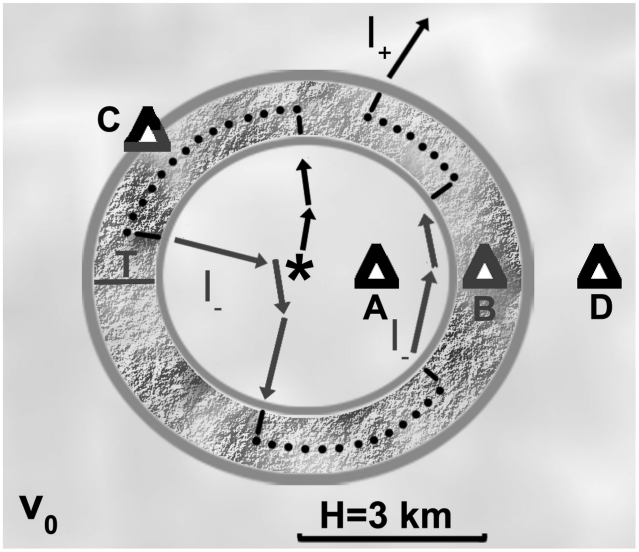

Figure 9. Sketch of medium and example of the propagation of a particle after the inclusion of a rim of thickness T and radius $H = 3$ km. Station A (black triangle) is surrounded by the rim, station B (dark grey triangle) is located on the rim, station C (half dark grey and half black triangle) is near the outer side of the rim, and station D (black triangle) is in the medium outside the rim. The original intensity flux (black arrows from the source) splits into a forward intensity flux, propagating outside of the rim (I_+, black arrow) and a backward intensity flux, propagating inside the medium surrounded by the rim (I_-, light grey arrows). The process can be repeated more than once until I_- exists. The dotted black lines are the two arcs travelled by the particle inside the rim before I_+ is created. The rim is characterized by a different scattering texture, and by its section T.

particularly remark the importance of the last parameter to model the intermediate peaks in coda intensities.

4.1 Propagation in a diffusive slab

Our source configuration simulates an extended source. A particle entering the highly scattering slab has a negligible probability to escape from it ballistically. More likely, the particles are transported diffusively inside the rim and escape after a typical propagation time, equal to the residence time or Thouless time of the waves as defined below. The transport mean free path associated to a diffusion step in the slab $(l^*)^r$ (obtained from the corresponding diffusion constant) is therefore much smaller than the transport mean free path for the rest of the medium, that is, $(l^*)^r \ll T \ll l^*_{p,s}$ (compare Tables 2 and 6). For simplicity, we do not differentiate between P and S energies inside the slab and consider a scalar approximation: this is well justified since the total energy satisfies a scalar diffusion approximation. We further assume that equipartition sets in rapidly inside the slab, so that upon escape the energy ratio $(\frac{E_p}{E_s})$ is equal to $\frac{V_s^2}{V_p^2}$. With these approximations we are able to find boundary

Table 6. Transport mean free path and diffusion constant in the diffusive rim. The parameters are deduced by the scattering coefficients proposed by Tramelli *et al.* (2006).

$\frac{km^2}{s}$	3 Hz	18 Hz
$(l^*)^r$	0.15	0.45
D^r	0.1	0.3

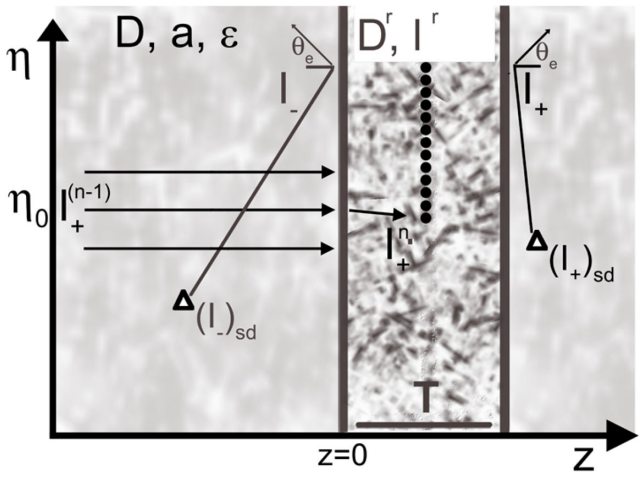

Figure 10. The annular boundary of Fig. 9 is locally approximated to a slab of distributed scatterers having higher scattering power. The asterisk represents the source location. The light grey medium has the same statistical characteristics of the one in Fig. 4 (the diffusion constant D, correlation length a, and mean fluctuation of the velocity wavefield ϵ). The boundary has different statistical characteristics [$D^r \ll D$ and mean (transport mean) free path $(l^*)^r$]. The last scattering event in the original medium is labelled as $(n-1)$; the corresponding intensity flux is I_+^{n-1}. The incident intensity at the inner side of the rim splits into a forward and a backward intensity flux. The first forward scattering event after the boundary (n) corresponds to the intensity flux I_+^n; we do not record the corresponding intensity at the station. The intensities recorded at the stations (triangles) are $(I_+)_{sd}$ (in case the particle is only recorded at stations outside of the rim) or $(I_-)_{sd}$ (if the particle still propagates in the circled region, and is only recorded inside the rim). The transverse position where the particle escapes (dotted line) and the escape angle θ_e are statistically modelled, depending on the residence time τ in the slab.

conditions for the multiple scattering contribution of the diffuse intensity (I_D, eq. 14).

Based on these assumptions we consider eq. (14) giving the specific diffuse intensity in the general 2-D case. This expression can be derived from the Radiative Transfer equation when the flux anisotropy is weak. If we separate the strongly scattering slab from the original medium we can set boundary conditions at $z = 0$ and $z = T$ (see Fig. 10) in the scalar approximation; from Akkermans & Montambaux (2007, pp. 172–175) we derive the 2-D equivalent of these boundary conditions

$$I_D(T) + \frac{\pi (l^*)^r}{4} \frac{\partial I_D}{\partial z} \,|_{z=T} = 0 \tag{23a}$$

$$I_D(0) - \frac{\pi (l^*)^r}{4} \frac{\partial I_D}{\partial z} \,|_{z=0} = 0 \tag{23b}$$

where $\frac{\pi (l^*)^r}{4}$ is the 2-D extrapolation length l_e, much smaller than T. These boundary conditions are only approximately correct and imply that the corresponding energy densities approximately vanish at a distance l_e from the slab boundary, and that the scattering inside the slab is much more intense than its surroundings.

We write the solution of the diffusion equation (E_D^r) with the boundary conditions given by eq. (23) for a flux incident at a point on the inner slab side of coordinates $z = 0$ and η_0 (Fig. 10) as

$$E_D^r(\vec{r}, \vec{r_0}, t) = \frac{\exp\left[-\frac{(\eta-\eta_0)^2}{4D^r t}\right]}{\sqrt{4\pi D^r t}} C_n, \tag{24}$$

Downloaded from http://gji.oxfordjournals.org/ at University of Edinburgh on December 28, 2013

where C_n is

$$C_n = \sum_{n=0}^{n=\infty} c_n \left[\cos(k_n z) + \frac{1}{k_n l_e}\sin(k_n z)\right] \times \left[\cos(k_n z_0) + \frac{1}{k_n l_e}\sin(k_n z_0)\right] \exp\left(-D^r k_n^2 t\right) \quad (25)$$

and k_n is the momentum of the nth root eigenvalues of the diffusion equation (υ). As a rule of thumb, usually accepted in optics, we assume that the injection position z_0 for the intensity is 1 mean free path, for incidence perpendicular to the slab.

The normalization constants c_n are given by

$$c_n^{-1} = \frac{T}{2}\left\{\left[1 + \frac{1}{k_n^2 l_e^2} + \frac{1-\cos(k_n T)}{k_n T k_n l_e}\right] + \frac{\sin(2k_n T)}{2k_n T}\left(1 - \frac{1}{k_n^2 l_e^2}\right)\right\}, \quad (26)$$

where $k_n = \frac{\upsilon}{T}$. υ_0 is the lowest lying eigenvalue, solution of the following equation:

$$\tan\upsilon = \frac{\frac{2\upsilon l_e}{T}}{\left(\frac{\upsilon l_e}{T}\right)^2 - 1}. \quad (27)$$

If we assume $\frac{l_e}{T} = 0.1$ we can solve eq. (27) numerically, obtaining $\upsilon_0 \cong 2.63$ and $k_0 = \frac{2.63}{T}$.

We implement the diffusive boundary of finite thickness in the Monte Carlo simulation by treating the total elastic energy as a single scalar quantity obeying the diffusion equation, hence considering only the first momentum solution k_0. eq. (24) connects the starting transverse position of each incident particle (η_0) with the escape transverse position on the sides of the slab (η). The diffuse intensity (I_{D}) takes the form

$$I_{\mathrm{D}}(\vec{r}, \vec{r_0}, t) \cong \frac{\exp\left[-\frac{(\eta-\eta_0)^2}{4D^r t}\right]}{\sqrt{4\pi D^r t}} \exp\left(-D^r k_0^2 t\right). \quad (28)$$

The slab is then uniquely characterized by its residence time τ (Akkermans & Montambaux 2007, p. 156) given by eq. (28)

$$\tau = \frac{1}{D^r k_0^2} \cong \frac{T^2}{D^r 2.63^2}. \quad (29)$$

This time is the average characteristic time spent by a particle propagating inside the slab. Because the intensity profile is symmetric (Fig. 10) if we consider only the first mode of the diffusion solution the value of z_0 is irrelevant, and the probability of transmission at $z = T$ and reflection at $z = 0$ are equal. Hence, we expect a diffusive intensity flux having opposite direction with respect to the incident flux near $z = 0$, whose amplitude is comparable with the incident intensity flux.

Finally, we obtain using eq. (14) that the probability P_{e} to escape the slab at an angle θ_e (Fig. 10) is given by

$$P_{\mathrm{e}}(\theta_{\mathrm{e}}) = \frac{1}{4}\left[1 + \frac{4}{\pi}\cos(\theta_{\mathrm{e}})\right]\cos(\theta_{\mathrm{e}}) \quad (30)$$

for $\theta_{\mathrm{e}} \in]-\pi/2, \pi/2[$. The corresponding cumulative density function $\mathrm{CDF_e}$ is

$$\mathrm{CDF_e}(\theta_{\mathrm{e}}) = \frac{1}{4}\left[\sin(\theta_{\mathrm{e}}) + \frac{\sin(2\theta_{\mathrm{e}})}{\pi} + 2\left(1 + \frac{\theta_e}{\pi}\right)\right] \quad (31)$$

and can be used to find the escape angle with a table-lookup method.

4.2 Implementation of the diffusive reflection and transmission from a slab of finite thickness

We locally approximate the rim by a diffusive slab of thickness T. In Fig. 9, the particle produced at the source is reflected twice before it escapes from the rim. Fig. 10 zooms in on the point of the rim where the incident flux crosses the inner side of the rim. A probabilistic interpretation of eq. (28) provides the escape time and position of a particle that enters the slab. The escape time t_{e} follows an exponential distribution with parameter τ. Once t_{e} has been randomly selected, the escape position (η) is determined by simulating a Gaussian distribution centred around the entrance point η_0, with variance $2D^r t$ and the inverse distribution method. The diffusivity of the slab is D^r (Table 6) obtained by decreasing the diffusion constant of two (18 Hz) and three (3 Hz) orders of magnitude, respectively. The ratio between D^r and D now controls the behaviours of the seismic envelopes at different frequencies.

In our configuration η is transformed into the angular coordinate with respect to the polar coordinate system with the centre in the epicentre and H as radius of the rim (Fig. 9). The probability to contribute to the I_- or the I_+ flux is the same. The escape angle is set with a table look-up method, where the angles are obtained from the cumulative density function of eq. (31). We finally use equipartition (see eq. 16) to determine whether the escaping particle is a P- or S-wave particle. As observed by Papanicolaou *et al.* (1996a,b) assuming constant velocities in the slab this will mainly be an S-wave particle ($E_s \approx 4E_p$).

5 RESULT OF THE MONTE CARLO SIMULATION IN THE PRESENCE OF A HIGHLY SCATTERING RIM

Our hypothesis is that the theory developed in section 4 models scattering propagation in the whole caldera, particularly the effect of energy trapping and the enhancement of diffusion. Hence, we study the effect of embedding a single highly scattering structure in the medium in order to model the anomalous intensities in the coda array envelopes. In Fig. 9 we consider a simplified close annular boundary of radius $H = 3$ km containing the centre of the caldera, and approximately following the rim-signature at 1.5 km depth as shown by the scattering tomography of Tramelli *et al.* (2006). When implemented in the Monte Carlo simulation such a boundary produces retarded energy, visible in the intermediate and late coda. The contribution is always dependent on the extrapolation length, which varies with frequency ($l_{\mathrm{e}} = 0.3$ km and 1 km at 18 and 3 Hz, respectively) with larger sections producing larger escape positions along the ring with respect to the incident positions. The boundary conditions manifest themselves through peaked amplitude increases or general broadening, depending on the boundary–station distance.

5.1 Station surrounded by the rim-boundary

We assume that the array envelopes calculated at station W2 (1.6 km source–receiver distance) are typical envelopes for a station surrounded by the rim. At 18 Hz the correlation between the synthetic envelope (black line, Fig. 11a) for $T = 2$ km and the array envelope (grey bold line) is striking. The wavefield propagates from the source inside the original medium until it crosses the inner side of the rim, which separates out the forward and the backward intensities. The best results with forward modelling are obtained for $T = 2$ km. The intermediate coda broadening is mainly due to the I_- flux, produced on the inner side of the rim (Fig. 9) while the

Downloaded from http://gji.oxfordjournals.org/ at University of Edinburgh on Decem

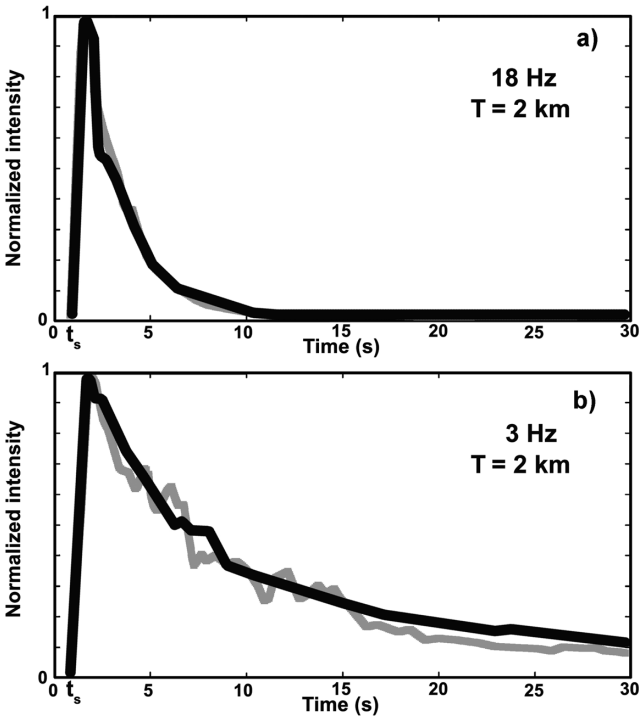

Figure 11. (a) Result of the simulation for a station surrounded by an annular rim having radius 3 km at 18 Hz (station A, Fig. 9). The continuous black line corresponds to the Monte Carlo envelope for a rim of thickness $T = 2$ km. The envelope at station W2 is shown in bold grey. The parameters ruling propagation in the original medium are shown in Tables 1 and 2. (b) The same comparison for frequencies of 3 Hz.

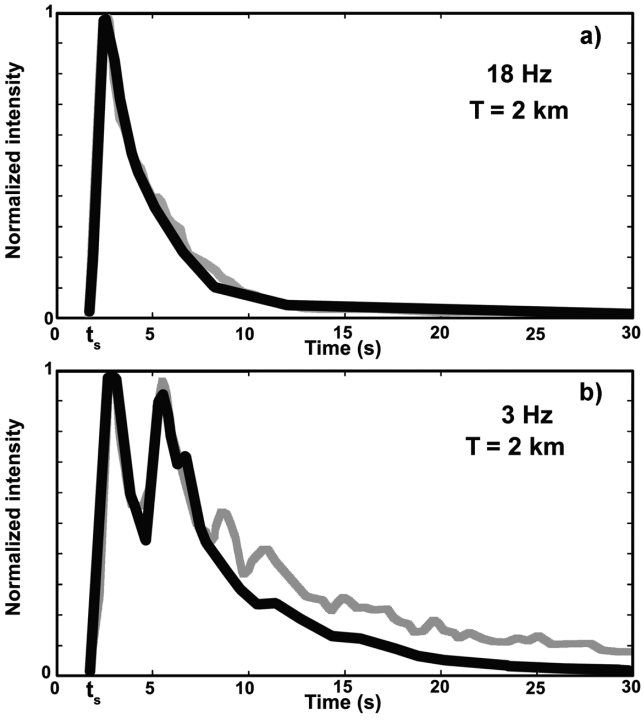

Figure 12. (a) Result of the simulation for a station located inside the annular rim having radius 3 km at 18 Hz (station B, Fig. 9). The continuous black line shows the Monte Carlo envelope for a rim of thickness $T = 2$ km. The envelope at station W20 is shown in bold grey. (b) The same comparison for frequencies of 3 Hz.

drastic exponential coda decrease is caused by the I_+ flux, quickly escaping from the outer side of the rim, and lost through the boundary at $L = 10$ km. Hence, the backward intensity flux increases the intensities at intermediate times producing general coda envelope broadening. The station–rim distance is nevertheless larger than the extrapolation length l_e at 18 Hz ($l_e = 0.3$ km) and 3 Hz ($l_e = 1$ km) and no anomalous high amplitudes are visible in the intermediate coda.

At 3 Hz the array envelopes also correlate well with the synthetic envelopes obtained for $T = 2$ km (Fig. 11b, black continuous line). As shown in Figs 6 and 7a statistical simulation without strong lateral variations of the scattering properties is unable to model the broadening of the real envelopes with the chosen parameters. In this frequency range the *S*-wave mean free path is much larger than the source-to-boundary distance (see Table 2). The wavefield interacts with the inner side of the rim after one step of the simulation, creating a second intensity source located on the interface of the rim. The envelope at a station surrounded by the rim is characterized by strong broadening if it is at a distance comparable to l_e from the boundary, where $l_e = 1$ km at 3 Hz. While at 18 Hz the rim acts as a secondary source, with the primary source still visible in the envelope, at 3 Hz the rim becomes the main diffuse source extended to a large area after a few seconds from the direct arrival. Its effects are evident in the intermediate coda, while late coda is controlled by isotropic scattering.

5.2 Station in proximity of the rim

The stations located within close range of the rim (stations B and C, Fig. 9) show different synthetic envelope behaviours at 18 Hz, dependent on how near they are with respect to one of the sides of the rim itself (compare Figs 12a and 13a).

We start considering the station confined inside the rim (station B, Fig. 9). The black continuous line in Fig. 12(a) is the result of the Monte Carlo simulation for $T = 2$ km, a source–receiver distance of 3 km, and a source–rim distance of 2 km (distance from the inner interface of the rim). The calculated array envelope shown in the same figure (grey bold envelope) is the transverse envelope recorded at station W4 (Fig. 1). At 18 Hz the interaction of the incident wavefield with the inner side of the rim produces the fluxes enhancing the coda broadening. However, the station is still far from both sides of the rim, and the recorded intensities after the interaction with the sides of the rim are dependent on the cumulative distribution function given by eq. (31). A more precise model should take into account the distribution of intensity inside the slab, having its maximum at the centre of the rim, and should disregard the incident flux, which is still included in the envelope. The distance between station B and each interface of the rim rules the broadening of the envelope, but does not produce a second broadened peak in the coda.

At 18 Hz local anomalous intensities in the intermediate coda are much more important if we locate the station near the inner (or outer) side of the rim (station C, Fig. 9). The synthetic envelope presents a large anomalous intensity in the intermediate coda (black continuous line in Fig. 13) for $T = 3$ km). The source–station distance in this case is 3.8 km. The onset of this peak is broadened in time, and cannot be correlated with the presence of a source precisely located in space. Indeed, it is the result of the transmission of the incident wavefield on the part of the external interface located near the station. The synthetic data match the transverse array envelope shown with a grey bold line in the same figure (station W20,

Downloaded from http://gji.oxfordjournals.org/ at University of Edinburgh on December 28, 2013

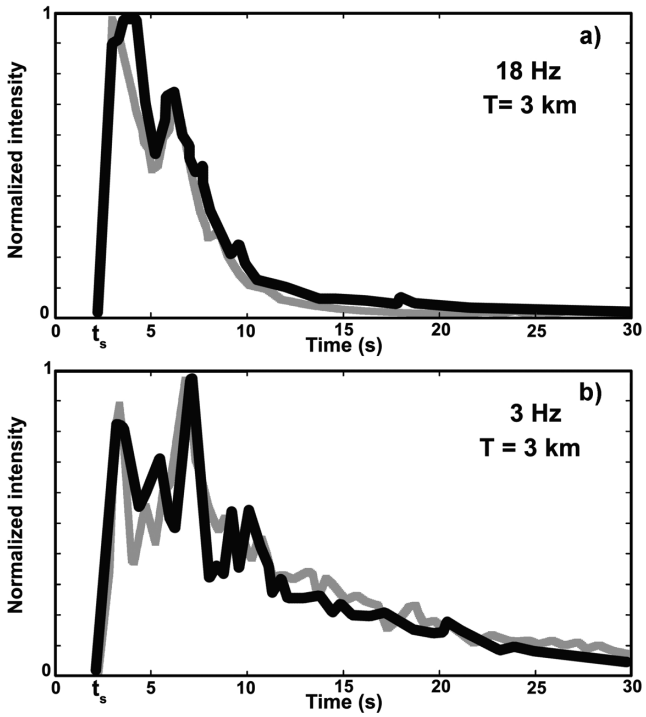

Figure 13. (a) Result of the simulation for a station located on the outer side of an annular rim having radius 3 km at 18 Hz (station C, Fig. 9). The continuous black line shows the Monte Carlo envelope for a rim of thickness $T = 3$ km. The envelope at station W4 is shown in bold grey. (b) The same comparison for frequencies of 3 Hz.

Fig. 1). The change in thickness ($T = 3$ km) is necessary to match the broadening and the onset of the second peak. If compared with the model required to match the envelope at station W4 it suggests a clear difference in the shape of the rim. More generally, our circular rim model is too simple to model every envelope in the caldera, and a second highly scattering object could be located in the direction between the source region and station W20. The total envelope broadening for the model at station W20 is not only controlled by the thickness of the rim, as for station W4. The presence of a local interface near one of the stations strongly affects its recordings, and the two envelopes in Fig. 12(a) and Fig. 13(a) are practically uncorrelated.

The array envelopes at stations W4 and W20 are shown in Figs 12(b) and 13(b) for the 3 Hz frequency band (grey continuous line). No particular difference can be observed in the two envelopes except for the onset of the second large intensity peak in the intermediate coda (which appears at later lapse time at station W20). The Monte Carlo envelopes obtained at the two stations (black lines in Figs 12b and 13b) also show this anomalous peak in the intermediate coda. The synthetic envelope of Fig. 12(b) is generally more noisy, again due to its proximity to the side of the rim. In both cases the boundary controls the intermediate coda envelope, enhancing anomalous intensities which are recorded similarly in the whole rim (see e.g. stations W4, W20 and W21 in Fig. 2). At 3 Hz the rim acts as a reflecting wall, which produces similar results at distant stations. The energy is reflected or transmitted by the rim, and finally lost outside of the region, and the intensities at any station near the rim are ruled by the boundary conditions.

These observations can be explained considering that at 3 Hz the *S*-wave mean free path is always much larger than the source-to-boundary distance (see Table 2). As in section 5.1 the interaction of the incident wavefield with the sides of the rim produces two energy fluxes (I_+ and I_-) which are now immediately detected at both stations. Hence, they increase coda intensities at large lapse times and enhance the broadened anomalous coda peak of maximum intensity comparable with the direct one. At 18 Hz the anomalous intermediate coda peak only affects one of the stations (W20) clearly suggesting a major contribution of this highly scattering anomaly at this station.

5.3 Station outside the rim

As we increase the source–station distance the inclusion of a single change in the scattering texture provides a good model of the complete coda envelope broadening, and gives useful hints for understanding the structure of the caldera as well as the main sources affecting distant station intensity measurements. Station D in Fig. 9 is located at 4.5 km distance from the source and at 0.5 km distance from the outer interface of the rim (hence, in the medium outside of the rim). The synthetic envelopes calculated at this station are shown in Fig. 14 (black continuous line) together with the array envelopes (bold grey lines) at station W3 (Figs 1 and 2).

At 18 Hz the continuous black curve mainly represents the intensity flux produced after crossing the rim. We observed that the total average intensity of the envelope is greatly lowered with respect to the ones at other stations (see section 5.4). Namely, it is the sum of the incident flux produced at the hypocentres and of the I_- and I_+ produced on the sides of the rim. Actually, with our model, the I_+ flux is the only extended circular source (depicted by the outer side of the rim) recorded at the station. The broadened envelope is not characterized by a single anomalous intensity peak, and the maximum amplitude, as well as the *S*-wave arrivals are delayed with

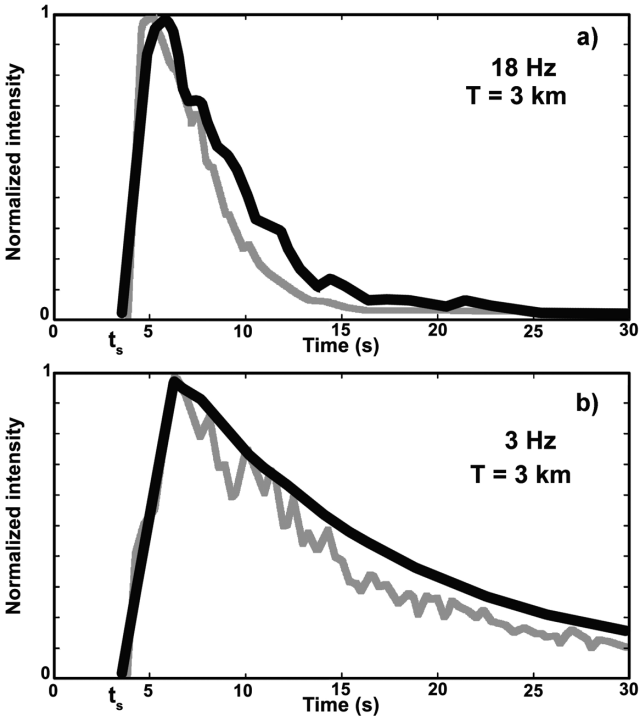

Figure 14. (a) Result of the simulation for a station located outside of the annular rim having radius 3 km at 18 Hz (station D, Fig. 9). The continuous black line shows the Monte Carlo envelope for a rim of thickness $T = 3$ km. The envelope at station W3 is shown in bold grey. (b) The same comparison for frequencies of 3 Hz.

Downloaded from http://gji.oxfordjournals.org/ at University of Edinburgh on Decem

respect to the *S*-wave direct onset calculated with the standard ray tracing technique.

The simplistic single-boundary model we propose cannot well model the coda array envelope at 3 Hz (Fig. 14b). Since the *S*-wave mean free path is larger than the source-to-boundary distance we assume that the wavefield also samples other boundaries in proximity of the station, or the horizontal interface between 3 and 4 km depth. However, as lapse time increases, the effect of (at least) a single drastic change in the scattering texture is necessary to model the average coda envelope behaviour.

5.4 Limitations, assumptions and discussion

The first and most important shortcoming of this theory is that in eq. (25) we only use the first term of the sum, the first mode of the diffusion solution. Disregarding the other modes we obtain equal probabilities of transmission and reflection, as well as a simplified late time approximation for the diffuse intensity, given by eq. (28). However, even the effect of first order terms in eq. (25) is not negligible: for a slab of 10 times l_e (approximately our case at 18 Hz) the reflection probability becomes higher than the transmission probability (72 and 28 per cent, respectively). Considering the other terms also means changing eqs (30) and (31) with more complex expressions. To simplify the simulation, we preferred to neglect the higher modes of the diffusion approximation, which mainly contribute at short times. We must also discuss a second shortcoming: we consider velocity and scattering coefficient as constant in our depth range, and no intrinsic attenuation. Our particular source geometry tries to smooth these effects but, if strong horizontal velocity variations (such as the one at 3 km depth) are still present, part of the energy will be lost in the deeper layer, as shown by Parsieglia & Wegler (2008).

In Figs 15(a) and 16(a), we show the amplitude decrease with distance, relative to station W2, which is also affected by the presence of the circular rim in the model (Figs 15b and 16b, left). We check the synthetic amplitude decrease by using the relative amplitude decrease of the maximum of the envelope multiplied for geometrical spreading and an exponential damping factor (Figs 15c and 16c, total average quality factor of 50 at both frequencies) which accounts for the higher attenuation at lower depths (De Siena *et al.* 2010). The effect of the highly scattering rim on the maximum amplitude is still secondary at stations W2 and W4, producing only general broadening. Starting from station W20 our model produces severe differences between the 18 and 3 Hz frequency bands (Figs 15a and 16a). At 18 Hz the rim enhances and broadens the envelope, but the maximum amplitude decrease at station W20 is much higher in the data than in the synthetics. At 3 Hz, we record larger amplitudes at station W20 than at station W4, even if W4 is nearer to the epicentre area (Fig. 16a). At station W3, the maximum amplitude is produced

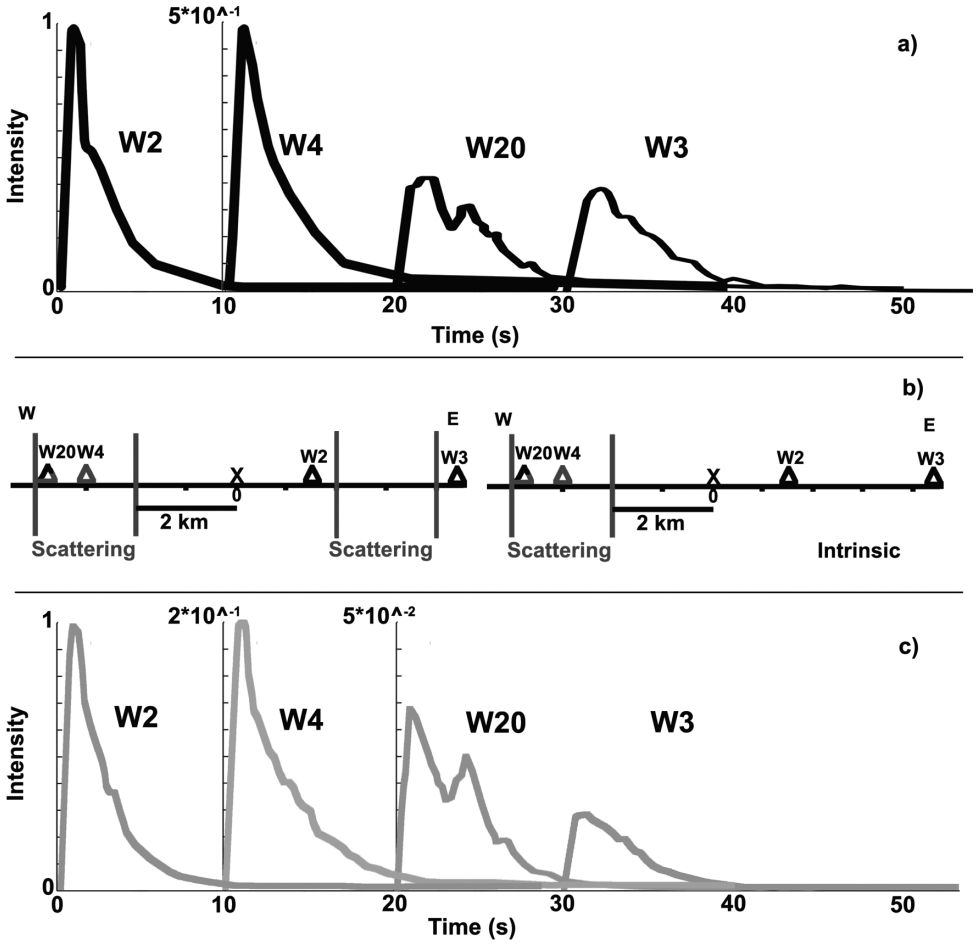

Figure 15. (a) Amplitude decrease with distance, and with respect to the amplitude at the nearest station (W2) at 18 Hz. (b) Left: Sketch of the source and stations with the proposed closed annular model. Right: Sketch of the source and stations with the model proposed by De Siena *et al.* (2011) assuming predominant scattering attenuation in the Western part of the caldera. (c) Amplitude decrease in the data considering geometrical spreading and a total quality factor of 50 in order to lower direct phases.

Downloaded from http://gji.oxfordjournals.org/ at University of Edinburgh on December 28, 2013

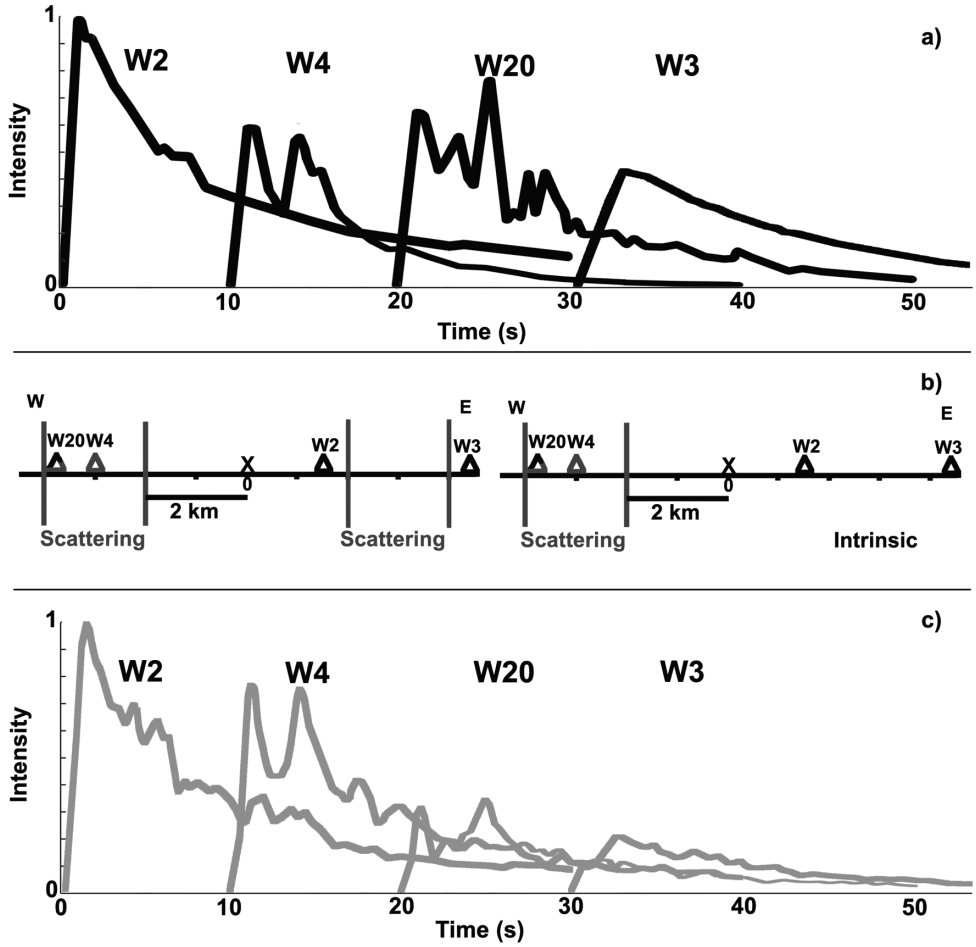

Figure 16. Same as Fig. 15 for 3 Hz.

by the rim, and remains at the same level of station W20 at both frequencies, even if at 3 Hz it is as high as at station W4 .

The maximum amplitude decrease looks realistic if we consider stations W2 and W4. Especially at 3 Hz, at the other stations the modelled amplitudes are too large compared with the data amplitude decrease. The assumption of strong scattering requires the source–receiver distance to be larger than the mean free path (Wegler & Lühr 2001) which can be the case only at 18 Hz. In order to apply radiative transfer theory the mean free path should be much larger than the wavelength λ. This is also the case for 18 Hz ($\lambda = 0.083$ km) but not for 3 Hz, where $\lambda = 0.5$ km (both λ are obtained using an average *S*-wave velocity of 1.5 km s^{-1}). The results at 18 Hz could be matched with the inclusion of intrinsic attenuation, which quickly lowers the coda envelopes, and is not considered in the coda modelling. The bias between *T* and intrinsic absorption must be considered in order to obtain a better scattering model for the caldera. The inhomogeneity in the amplitude decrease in the 3 Hz frequency range (Fig. 16a) as well as the results obtained so far reveal that a circular model is not the best possible model for the highly scattering object, but in order to get a best-fitting model of the envelopes singles station observations of total amplitude will be necessary.

The inclusion of a strongly scattering rim reflecting or transmitting energy is a method to model energy entrapment and resonant scattering, which produces most of the energy recorded at the larger distances from the source, and is valid if coda consists mainly of *SS* scattered waves, as we expect at large lapse times. What we derive from Figs 15(a) and 16(a) is that we cannot reproduce a realistic coda broadening together with the correct amplitude decrease with a circular rim-model at every station. In the centre of Figs 1 and 2 we report the results of the separation between intrinsic and scattering attenuation obtained in this depth and frequency ranges by De Siena *et al.* (2011). We speculate that a semicircular, or a half-space model, with higher power in the western caldera (right-hand panel, Figs 15b and 16b) could better model both envelope broadening and amplitude decay in both frequency ranges, especially at large distances from the source. Also, the hydrothermal basin located below Pozzuoli (near the source region) could be modelled with resonant scattering with intrinsic attenuation. This could easily explain, for example, the lowest *S*-wave direct amplitudes of the caldera, recorded at station W11 (Vanorio *et al.* 2005; De Siena *et al.* 2010).

Diffusivities are critical parameters for our model, since the amplitudes of the intermediate coda at both frequencies are controlled by the ratio between diffusion constant of the rim and diffusion constant of the medium in which the rim is embedded. This large contrast is responsible for the whole energy envelope recorded at station W3. If our circular model would be true, no actual direct arrival should be recorded for this envelope, produced only by the diffusively scattering rim. In this case the stack, done on the base of theoretical *S*-wave arrivals, is obviously wrong. We need higher diffusivity ratios to model coda broadening at 3 Hz ($\frac{D^r}{D} = 0.0003$) than at 18 Hz ($\frac{D^r}{D} = 0.003$, where D and D^r are shown in Tables 2 and 6, respectively). In our interpretation, such large diffusion contrasts to model envelopes confirm the inapplicability of the standard Born

Downloaded from http://gji.oxfordjournals.org/ at University of Edinburgh on Decem

description, especially at 3 Hz, as well as the presence of resonant scattering, which can generally explain the small values of the diffusion constant of seismic waves reported in volcanic areas (Margerin 2013).

We reiterate that our aim is not to obtain a unique, best-fitting scattering model for Campi Flegrei, a scope which would require a complete inversion for several statistical parameters of the original medium (even if we show that, considering the mean free path, a realistic variation of the correlation length does not lead to significative differences). More simply, we could consider directly the transport mean free path, and not the mean free path, as the quantity controlling propagation in the homogeneous model. In this paper, however, we assess the difficulty of simulating the envelopes in the caldera with the standard description of Radiative Transfer Theory in terms of Born scattering coefficients (e.g. Przybilla *et al.* 2006; Yamamoto & Sato 2010). In addition, we cannot obtain the late-coda peaks in the intermediate coda, only visible at same stations in the western part of the caldera, without a drastic local change in the properties of the medium, with an increase of the scattering power, wether we consider the mean free path or the transport mean free path. The theory developed in this work is applicable even outside the limits of the diffusion equation.

6 CONCLUSIONS

The inclusion of a single reflective diffusive boundary of large scattering power in a 2-D Monte Carlo scattering simulation is able to describe intensity propagation in a small-scale heterogeneous volcanic medium without topography, and in our particular source–station configurations. In our approach three quantities control the coda envelope behaviour: the ratio between the *S*-wave mean free path (36 and 1 km for 3 and 18 Hz, respectively) and the source-to-boundary distance (around 3 km from its centre) the rim thickness (between 2 and 3 km) and the ratio between diffusivity of the slab and diffusivity of the background medium (10^{-3} and 10^{-2} at 3 and 18 Hz, respectively).

We demonstrate by means of Monte Carlo simulations and comparison with real envelopes that, if a deterministic approach provides unrealistic models of waveform envelopes, a totally stochastic one based on Monte Carlo simulations with typical lithospheric parameters is also imprecise, if boundary conditions are not taken into account. These boundary conditions manifest themselves as a secondary diffusive extended source, that controls intermediate and late coda behaviour, and strongly depend on frequency and boundary–station distance. We show that we cannot model the sharp intermediate coda increases in the Western part of the caldera without spatially dependent changes in the scattering properties of the medium, and, more generally, that a homogeneous model with typical lithospheric parameters is able to provide information on the form and duration of the envelopes, but a diffusive contribution is still necessary to efficiently model the whole envelope duration.

These results have striking consequences on volcano seismology as well as on the understanding of the seismic structure of the Campi Flegrei caldera. They provide data confirming the presence of resonant scattering, which generally explains the small values of the diffusion constant of seismic waves reported in volcanic areas. The first-order modelling of these effects clearly localizes the anomaly west of the source region, and the geological characteristics of the scattering object can be investigated by a complete inversion of the scattering and attenuation parameters. Finally, the inclusion of such effects in tomography codes represents a new strategy for the application of full waveform tomography techniques in volcanic regions, and our results can provide a better understanding of the complex physical processes affecting interferometric measurements in high-contrast media.

ACKNOWLEDGEMENTS

This work was carried out under the HPC-Europa2 project (project number: 228398) with the support of the European Commission Capacities Area-Research Infrastructures Initiative. We thank the whole staff at EPCC (Edinburgh Parallel Computing Centre) in Edinburgh and particularly Dr. Adam Carter for their help in both developing and parallelizing the code. The challenging comments and suggestions of the editor and two anonymous reviewers helped both in focusing the aim and in overcoming the strong limits of a previous version of the paper.

REFERENCES

Aki, K. & Ferrazzini, V., 2000. Seismic monitoring and modeling of an active volcano for prediction, *J. geophys. Res.,* **105,** 16 617–16 640.

Akkermans, E. & Montambaux, G., 2007. *Mesoscopic Physics of Electrons and Photons,* 1st edn, Cambridge University Press.

Aster, R., Meyer, R., Natale, G.D., Martini, M., Del Pezzo, E., Iannaccone, G. & Scarpa, R., 1989. Seismic investigation of the Campi Flegrei: a synthesis and summary of results, in *Volcanic Seismology, Proc. Volc. series III,* eds Aki, K., Gasparini, P. & Scarpa, R., Springer Verlag, pp. 462–483.

Battaglia, J., Zollo, A., Virieux, J. & Dello Iacono, D., 2008. Merging active and passive data sets in traveltime tomography: the case study of Campi Flegrei caldera (Southern Italy), *Geophys. Prospect.,* **56,** 555–573.

Binder, K. & Heermann, D., 2010. *Monte Carlo Simulation in Statistical Physics: An Introduction,* Vol. 80, Springer.

Block, L.V., 1991. Joint hypocenter–velocity inversion of local earthquake arrival time data in two geothermal regions, *PhD dissertation,* Massachusetts Institute of Technology, Cambridge, MA.

Chouet, B., 2003. Volcano seismology, *PAGEOPH,* **160,** 739–788.

Cormier, V.F. & Li, X., 2002. Frequency-dependent seismic attenuation in the inner core 2. a scattering and fabric interpretation, *J. geophys. Res.,* **107** (B12), doi:10.1029/2002JB001796.

De Lorenzo, S., Zollo, A. & Mongelli, F., 2001. Source parameters and three-dimensional attenuation structure from the inversion of microearthquake pulse width data: Qp imaging and inferences on the thermal state of the Campi Flegrei caldera (southern Italy), *J. geophys. Res.,* **106,** 16 265–16 286.

Del Pezzo, E., 2008. Seismic wave scattering in volcanoes, in *Earth Heterogeneity and Scattering Effects of Seismic Waves,* Vol. 50: Advances in Geophysics, Chap. 13, pp. 353–369, Elsevier.

Del Pezzo, E. & Bianco, F., 2013. A reappraisal of seismic Q evaluated in Campi Flegrei caldera. Receipt for the application to risk analysis, *J. Seismol.,* **17**(2), 829–837.

De Siena, L., Pezzo, E.D. & Bianco, F., 2010. Campi Flegrei seismic attenuation image: evidences of gas resevoirs, hydrotermal basins and feeding systems, *J. geophys. Res.,* **115**(B0), 9312–9329.

De Siena, L., Del Pezzo, E. & Bianco, F., 2011. A scattering image of Campi Flegrei from the autocorrelation functions of velocity tomograms, *Geophys. J. Int.,* **184**(3), 1304–1310.

Gusev, A.A. & Abubakirov, I.R., 1987. Monte-carlo simulation of record envelope of a near earthquake, *Phys. Earth planet. Inter.,* **49,** 30–36.

Gusev, A.A. & Abubakirov, I.R., 1996. Simulated envelopes of non-isotropically scattered body waves as compared to observed ones: Another manifestation of fractal heterogeneity, *Geophys. J. Int.,* **127,** 49–60.

Hennino, R., Tregueres, N., Shapiro, N.M., Margerin, L., van Tiggelen, B.A. & Weaver, R.L., 2001. Observation of equipartition of seismic waves, *Phys. Rev. Lett.,* **86**(15), 3447–3450.

Holliger, K. & Levander, A.R., 1992. A stochastic view of lower crustal fabric based on evidence from the Ivrea zone, *Geophys. Res. Lett.,* **19,** 1153–1156.

Downloaded from http://gji.oxfordjournals.org/ at University of Edinburgh on December 28, 2013

Hoshiba, M., 1991. Simulation of multiple–scattered coda wave excitation based on the energy conservation law, *Phys. Earth planet. Inter.,* **67,** 123–136.

Larose, E., Margerin, L., van Tiggelen, B.A. & Campillo, M., 2004. Weak localization of seismic waves, *Phys. Rev. Lett.,* **93,** 048501–048504.

Levander, A. & Nolet, G., eds, 2005. *Seismic Earth: Array Analysis of Broadband Seismograms,* Geophysical Monograph Series, American Geophysical Union, Washington, DC.

Lomax, A., Zollo, A., Capuano, P. & Virieux, J., 2001. Precise, absolute earthquake location under somma vesuvius volcano using a new three dimensional velocity model, *Geophys. J. Int.,* **146,** 313–331.

Margerin, L., 2006. Attenuation, transport and diffusion of scalar waves in textured media, *Tectonophysics,* **416,** 229–244.

Margerin, L., 2013. Diffusion approximation with polarization and resonance effects for the modelling of seismic waves in strongly scattering small-scale media, *Geophys. J. Int.,* **192**(1), 326–345.

Margerin, L. & Nolet, G., 2003. Multiple scattering of high-frequency seismic waves in the deep Earth: modeling and numerical examples, *J. geophys. Res.,* **108**(B5), 2234–2249.

Margerin, L., Campillo, M. & Tiggelen, B.V., 1998. Radiative transfer and diffusion of waves in a layered medium: new insight into coda Q, *Geophys. J. Int.,* **134,** 596–612.

Margerin, L., Campillo, M. & van Tiggelen, B.A., 2000. Monte Carlo simulation of multiple scattering of elastic waves, *J. geophys. Res.,* **105**(B4), 7873–7892.

Margerin, L., van Tiggelen, B.A. & Campillo, M., 2001. Effect of absorption on energy partitioning of elastic waves in the seismic coda, *Bull. seism. Soc. Am.,* **91,** 624–627.

Monnereau, M., Calvet, M., Margerin, L. & Souriau, A., 2010. Lopsided Growth of Earth's Inner Core, *Science,* **328**(5981), 1014–1017.

Neuberg, J. & Pointer, T., 2000. Effects of volcano topography on seismic broad–band waveforms, *Geophys. J. Int.,* **143,** 239–248.

Paasschens, J. C.L., 1997. Solution of the time-dependent Boltzmann equation, *Phys. Rev.,* **56**(1), 1135–1141.

Papanicolaou, G., Ryzhik, L.V. & Keller, J.B., 1996a. Stability of the P-to-S energy ratio in the diffusive regime, *Bull. seism. Soc. Am.,* **86,** 1107–1115.

Papanicolaou, G., Ryzhik, L.V. & Keller, J.B., 1996b. Stability of the P-to-S energy ratio in the diffusive regime, Erratum, *Bull. seism. Soc. Am.,* **86,** 1107–1115.

Parsieglia, N. & Wegler, U., 2008. Modelling of seismic energy transport at volcanoes with real topography and complex propagation medium, *J. Volc. Geotherm. Res.,* **171,** 229–236.

Przybilla, J. & Korn, M., 2008. Monte carlo simulation of radiative energy transfer in continuous elastic random media—three-component envelopes and numerical validation, *Geophys. J. Int.,* **173,** 566–576.

Przybilla, J., Korn, M. & Wegler, U., 2006. Radiative transfer of elastic waves versus finite difference simulations in two-dimensional random media, *J. geophys. Res.,* **111**(B0), 4305–4317.

Przybilla, J., Wegler, U. & Korn, M., 2009. Estimation of crustal scattering parameters with elastic radiative transfer theory, *J. geophys. Res.,* **111**(B0), 4305–4317.

Pujol, W.S. & Aster, R., 1990. Joint hypocentral determination and the detection of low-velocity anomalies. An example from the Phlegrean Fields earthquakes, *Bull. seism. Soc. Am.,* **80**(1), 129–139.

Ryan, H., 1994. Ricker, Ormsby, Klauder, Butterworth—a choice of wavelets, *Can. Soc. Explor. Geophys.Record.,* **19**(7), 8–9.

Rytov, S.M., Kravtsov, Y.A. & Tatarskii, V.I., 1987. *Principles of Statistical Radiophysics,* Vol. 4: Wave Propagation Through Random Media, Springer Verlag.

Ryzhik, L., Papanicolaou, G. & Keller, J.B., 1996. Transport equations for elastic and other waves in random media, *Wave Motion,* **24,** 327–370.

Saccorotti, G. *et al.*, 2007. Seismicity associated with the 2004–2006 renewed ground uplift at Campi Flegrei Caldera, Italy, *Phys. Earth planet. Int.,* **165,** 14–24.

Saito, T., Sato, H., Ohtake, M. & Obara, K., 2005. Unified explanation of envelope broadening and maximumamplitude decay of high–frequency seismograms based on the envelope simulation using the Markov approximation: Forearc side of the volcanic front in northeastern Honshu, Japan, *J. geophys. Res.,* **110**(B1), B01304, doi:10.1029/2004JB003225.

Sato, H., 1977. Energy propagation including scattering effects: single isotropic scattering approximation, *J. Phys. Earth,* **25,** 27–41.

Sato, H. & Fehler, M.C., 1998. *Seismic Wave Propagation and Scattering in the heterogeneous Earth,* Springer Verlag.

Sato, H., Fehler, M. & Saito, T., 2004. Hybrid synthesis of scalar wave envelopes in two-dimensional random media having rich short-wavelength spectra, *J. geophys. Res.,* **109**(B0), 6303–6314.

Sato, H., Fehler, M.C. & Maeda, T., 2012. *Seismic Wave Propagation and Scattering in the heterogeneous Earth: Second Edition,* Springer.

Sens-Schönfelder, C., Margerin, L. & Campillo, M., 2009. Laterally heterogeneous scattering explains lg blockage in the Pyrenees, *J. geophys. Res.,* **114**(B7), B07309, doi:10.1029/2008JB006107.

Shapiro, S.A. & Hubral, P., 1999. *Elastic Waves in Random Media, Fundamentals of Seismic Stratigraphic Filtering,* Springer.

Shiomi, K., Sato, H. & Ohtake, M., 1997. Broad–band power–law spectra of well–log data in Japan, *Geophys. J. Int.,* **130,** 57–64.

Thurber, C.H. & Eberhart–Phillips, D., 1999. Local earthquake tomography with flexible gridding, *Comput. Geosci.,* **25,** 809–818.

Tramelli, A., Pezzo, E.D., Bianco, F. & Boschi, E., 2006. 3D scattering image of the Campi Flegrei caldera (Southern Italy). New hints on the position of the old caldera rim, *Phys. Earth planet. Inter.,* **155,** 269–280.

Turner, J.A., 1998. Scattering and diffusion of seismic waves, *Bull. seism. Soc. Am.,* **88**(1), 276–283.

Vanorio, T., Virieux, J., Capuano, P. & Russo, G., 2005. Three-dimensional tomography from P wave and S wave microearthquake travel times and rock physics characterization of the Campi Flegrei Caldera, *J. geophys. Res.,* **110**(B03201), doi:10.129/2004JB003102.

Weaver, R.L., 1990. Diffusivity of ultrasound in polycrystals, *J. Mech. Phys. Solids,* **1** (38), 55–86.

Wegler, U., 2003. Analysis of Multiple Scattering at Vesuvius Volcano, Italy, Using Data of the TomoVes Active Seismic Experiment, *J. Volc. Geotherm. Res.,* **128,** 45–63.

Wegler, U., 2005. Diffusion of seismic waves in layered media: boundary conditions and analytic solutions, *Geophys. J. Int.,* **163,** 1123–1135.

Wegler, U. & Lühr, B.G., 2001. Scattering behaviour at Merapi Volcano (Java) revealed from an active seismic experiment, *Geophys. J. Int.,* **145,** 579–592.

Wu, R.S., 1985. Multiple scattering and energy transfer of seismic waves - Separation of scattering effect for intrinsic attenuation, I, *Geophys. J. R. astr. Soc.,* **82,** 57–80.

Yamamoto, M. & Sato, H., 2010. Multiple scattering and mode conversion revealed by an active seismic experiment at Asama volcano, Japan, *J. geophys. Res.,* **115**(B0), 7304–7317.

Yoshimoto, K., 2000. Monte-Carlo simulation of seismogram envelopes in scattering media, *J. geophys. Res.,* **B3**(105), 6153–6162.

Yoshimoto, K., Sato, H. & Ohtake, M., 1997. Three-component seismogram envelope synthesis in randomly inhomogeneous semi-infinite media based on the single scattering approximation, *Phys. Earth planet. Inter.,* **104,** 37–61.

Yoshimoto, K., Wegler, U. & Korn, M., 2006. A volcanic front as a boundary of seismic-attenuation structures in northeastern Honshu, Japan, *Bull. seism. Soc. Am.,* **96**(2), 637–646.

Zollo, A. & Bernard, P., 1991. Fault mechanisms from near-source data: joint inversion of S polarizations and P polarities, *Geophys. J. Int.,* **104,** 441–451.

Zollo, A., D'Auria, L., Matteis, R.D., Herrero, A., Virieux, J. & Gasparini, P., 2002. Bayesian estimation of 2-D P-velocity models from active seismic arrival time data: imaging of the shallow structure of Mt Vesuvius (Southern Italy), *Geophys. J. Int.,* **151,** 566–582.

Zollo, A. *et al.*, 2003. Evidence for the buried rim of Campi Flegrei caldera from 3-d active seismic imaging, *Geophys. Res. Lett.,* **30**(19), doi:10.1029/2003GL018173.

Zollo, A., Maercklin, N., Vassallo, M., Dello Iacono, D., Virieux, J. & Gasparini, P., 2008. Seismic reflections reveal a massive melt layer feeding Campi Flegrei caldera, *Geophys. Res. Lett.,* **35**(L112306), doi:10.1029/2008GL034242.

Downloaded from http://gji.oxfordjournals.org/ at University of Edinburgh on Decem